DOE-ET-53088-229

IFSR#229

ENHANCED ELECTRON STOCHASTICITY FROM DRIFT WAVES IN A SHEARED MAGNETIC FIELD

J.A. Robertson, W. Horton and D.I. Choi
Institute for Fusion Studies
The University of Texas at Austin
Austin, Texas 78712-1060

April 1986

Enhanced Electron Stochasticity From Electrostatic Waves in a Sheared Magnetic Field

J.A. Robertson, W. Horton, and D.I. Choi

Institute for Fusion Studies

University of Texas at Austin

Austin, Texas 78712

Abstract

Electron motion in a single electrostatic wave in a sheared magnetic field is shown to become stochastic in the presence of a second wave at an amplitude well below that obtained from the overlapping pendulum resonance approximation. The enhanced stochasticity occurs for low parallel velocity electrons for which the parallel trapping motion from $eE_{\|}/m$ interacts strongly with the $\mathbf{E}\times\mathbf{B}$ trapping motion due to the presence of magnetic shear. The single wave particle motion is given by a two parameter family of one degree-of-freedom Hamiltonians which bifurcate from a pendulum phase space to a topology with three chains of elliptic and hyperbolic fixed points separated in radius about the mode-rational surface. In the presence of a perturbing wave with a different helicity, electrons in the small parallel velocity regime become stochastic at an amplitude scaling as the fourth root of the wave potential. The results obtained for stochastic motion apply directly to the problem of the diffusion of electrons in drift waves.

I. Introduction

The motion of electrons across the confining magnetic field due to the $\mathbf{E}\times\mathbf{B}$ motion associated with low frequency drift modes is well recognized as an important mechanism for the anomalous transport in plasmas.[1] In addition to producing anomalous transport, the nonlinear motions of the electrons changes the stability of the drift modes by modifying the electron charge density response function at finite wave amplitudes.[2,3,4] Recent studies[5,6] of the nonlinear $\mathbf{E}\times\mathbf{B}$ motion of the particles in drift wave fields obtain results for the diffusion and resonance broadening when the perpendicular $\mathbf{E}\times\mathbf{B}$ motion decouples from the parallel motion. This decoupling approximation is adequate for describing the nonlinear motion of ions[5,6], but fails for the electron motion considered here.

The electron motion in drift waves is influenced both by the parallel acceleration, $eE_{\|}/m_e$, produced by the wave's electric field and the nonlinear $\mathbf{E}\times\mathbf{B}$ motion. In the presence of magnetic shear, Hirshman and Molvig[4] recognize that even the linear free-streaming electron motion directly couples to the nonlinear $\mathbf{E}\times\mathbf{B}$ motion. They show that with the approximation of constant parallel velocity, the nonlinear $\mathbf{E}\times\mathbf{B}$ motion reduces to the time-dependent pendulum Hamiltonian, with the canonical momentum equal to the radial coordinate and the canonical coordinate equal to the wave-particle phase variable. In this constant $v_{\|}$ approximation, the onset of stochasticity and the diffusion approximation are well known from the results of $1\frac{1}{2}$D Hamiltonian (pendula) theory.[7,8] The constant $v_{\|}$ approximation is good for electrons whose parallel kinetic energy in the wave frame is large compared with the electrostatic potential. For low parallel velocity electrons, where the difference between the parallel electron velocity $v_{\|}$ and the parallel phase velocity is of the order of the trapping velocity $v_0 = (e\phi/m_e)^{1/2}$, the approximation fails qualitatively, due to the strong coupling between the parallel and cross-field nonlinear motions.

In the present study, we analyze the drift motion of electrons in two electrostatic waves in the presence of magnetic shear. Collisions are ignored, and we assume given fields without attempting a self-consistent treatment. The problem of particle response to several drift modes associated with nearby rational surfaces of a tokamak provides the principle motivation for undertaking the study of this model. Our model is, however, quite self-contained and does not rely especially upon the origin of the modes. The model could equally well apply to electrostatic modes other than gradient-driven ones and parameter regimes vastly different from those relevent to tokamak physics. The only requirement is that the scales be such that the guiding-center description is valid.

In Sec. II., we show that the motion is governed by a 2D autonomous Hamiltonian system. The guiding-center equations of motion are presented in both non-canonical and canonical coordinates. We determine relevent scales for the coordinates and recast the equations of motion in terms of dimensionless variables. This simplifies the problem by greatly reducing the number of free parameters.

If only one wave is present, the system is integrable. In Sec. III., we discuss the features of the single wave orbits. We make a complete classification of all the orbit types which occur in the single wave problem. A bifurcation pattern of the single wave phase-space is derived as a function of two dimensionless parameters. The single wave electron orbits are too complex to be expressed in terms of elliptic functions.

Electrons in the low parallel kinetic energy regime display anomalous radial excursions over a scale determined by the geometric mean of the shear length L_s and the electron gyroradius calculated with the parallel trapping velocity, $\rho_0 = v_0/\omega_{ce}$, with v_0 given above. This radial scale-length thus displays $\phi^{1/4}$ dependence, as compared with the $\phi^{1/2}$ dependence of the pendulum regime considered by Hirshman and Molvig.

Particles located at the null-points of the electric field (i.e. $\mathbf{k} \cdot \mathbf{x} - \omega t = n\pi$) experience no parallel acceleration or cross-field drifts. If furthermore, the radial coordinate and parallel velocity are such that the Landau resonance condition $\omega = v_{\|} \hat{\mathbf{b}}(x) \cdot \mathbf{k} = v_{\|} k_y x / L_s$ is satisfied, then such particles will remain at the null-points of the electric field. These orbits are the stable and unstable fixed points of the phase space. The values of x and $v_{\|}$ at the fixed points stand in an inverse relationship to one another. The constant $v_{\|}$ approximation of earlier work focuses on the pendulum-like islands associated with the fixed points that occur for $v_{\|}$ large and x small. Little attention has been paid to the opposite case of islands occuring for small $v_{\|}$ and large x.

We find that for canonical momenta exceeding a certain value, the chain of elliptic and hyperbolic fixed points occuring in the pendulum approximation bifurcates into three chains of fixed points separated in radius about the rational surface. Depending on parameter values, these chains of fixed points may be interconnected in a variety of ways. We have paid particular attention to a lattice-like homoclinic orbit with energy equal to $e\phi$ which ties all three chains together. This orbit displays the maximum radial excursion for the single wave problem.

In the presence of a perturbing second wave, the complex pattern of homoclinic orbits joining the fixed points of the single wave problem become a stochastic web for small values of the perturbing wave amplitude. Orbits with energy equal to $e\phi$ are observed to be extremely fragile to the onset of chaos. Applying the overlapping resonance ideas[7,8,9] to our 2D system, in Sec. IV., we estimate the value of the wave amplitudes for global stochasticity from two neighboring drift waves. For amplitudes exceeding this critical value, computer experiments show radial diffusion of the electrons. From the dimensionless variables appropriate for this system, we are able to establish the scaling of the diffusion

coefficient $D_\perp$. In Sec. V., we give the summary and conclusions.

II. The Equations of Motion

We investigate the motion of an electron in a magnetic field with shear in the presence of two electrostatic plane waves. We assume magnetic and electric fields of the form

$$\mathbf{B} = B_0 \left[\hat{\mathbf{e}}_y \sin \frac{x}{L_s} + \hat{\mathbf{e}}_z \cos \frac{x}{L_s} \right], \tag{1}$$

$$\mathbf{E} = -\nabla \Phi, \tag{2}$$

$$\text{where} \quad \Phi = \phi_1 \cos(\mathbf{k}_1 \cdot \mathbf{r} - \omega_1 t) + \phi_2 \cos(\mathbf{k}_2 \cdot \mathbf{r} - \omega_2 t). \tag{3}$$

The wave-vectors $\mathbf{k}_1$ and $\mathbf{k}_2$ are taken to be non-parallel and to both lie in the y-z plane. The above choice of electrostatic potential neglects mode-coupling effects[10] and the radial structure (i.e. the x-dependence) of the modes[5,6]. The field of Eq. (1) is produced by a current $\mathbf{j} = \frac{cB_0}{4\pi L_s} [\hat{e}_z \cos(x/L_s) + \hat{e}_y \sin(x/L_s)]$. Our choice of B-field for the present model was motivated by the fact that it has the nice feature of a constant magnitude. The detailed form of the sheared B-field is, however, not especially important, since we are interested in values of x small compared with the shear length L_s.

We make a Galilean transformation to a reference frame moving with velocity $\mathbf{w}$ with respect to the lab frame. Denoting the transformed coordinates with primes, $\mathbf{r}' \equiv \mathbf{r} - \mathbf{w}t$. $\mathbf{w}$ is chosen so as to simultaneously solve $\omega_1 = \mathbf{k}_1 \cdot \mathbf{w}$ and $\omega_2 = \mathbf{k}_2 \cdot \mathbf{w}$; namely, we take $w_x = 0$, $w_y = (k_{2_z}\omega_1 - k_{1_z}\omega_2)/d$, and $w_z = (k_{1_y}\omega_2 - k_{2_y}\omega_1)/d$, where $d \equiv k_{1_y}k_{2_z} - k_{1_z}k_{2_y}$. With this choice, one finds that $\mathbf{k}_i \cdot \mathbf{r} - \omega_i t = \mathbf{k}_i \cdot \mathbf{r}'$ for $i = 1, 2$. Hence, the fields are time-independent in the transformed reference frame. Note that the transformation is not possible when $\mathbf{k}_1$ and $\mathbf{k}_2$ are parallel, since, in this case, $d = 0$. For non-relativistic $\mathbf{w}$, the fields in the wave-frame are given by $\mathbf{E}' = \mathbf{E} + c^{-1}\mathbf{w} \times \mathbf{B}$

and $\mathbf{B}' = \mathbf{B} - c^{-1}\mathbf{w} \times \mathbf{E}$. We ignore the induced magnetic field, taking $\mathbf{B}' = \mathbf{B}$, since $|\mathbf{E}| \ll B_0$. The importance of the wave frame for two $\mathbf{E} \times \mathbf{B}$ wave problem is pointed out by Hirshman.[11]

The guiding-center equations of motion for electron orbits are then given, in terms of the wave frame coordinates, by

$$\frac{dv'_{\|}}{dt} = -\frac{e}{m_e}\hat{\mathbf{b}} \cdot \mathbf{E}, \tag{4}$$

$$\frac{d\mathbf{r}'}{dt} = v'_{\|}\hat{\mathbf{b}} + \frac{c}{B_0^2}\left[\mathbf{E} + \frac{\mathbf{w} \times \mathbf{B}}{c}\right] \times \mathbf{B}, \tag{5}$$

where e is the magnitude of the electron charge, m_e is the electron mass, $\hat{\mathbf{b}}$ is the unit vector in the direction of the magnetic field, and $v'_{\|} = \hat{\mathbf{b}} \cdot d\mathbf{r}'/dt$ is the parallel velocity.

The guiding-center equations thus constitute a two-degree-of-freedom, autonomous, dynamical system with phase space coordinates $(v'_{\|}, x', y', z')$. We note that adding a third wave having wave-vector $\mathbf{k}_3$ in the y-z plane would, in general, preclude the possibility of finding a wave-frame where the fields are time-independent, since the additional condition $\omega_3 = \mathbf{k}_3 \cdot \mathbf{w}$ results in an overdetermined set of equations. Only in the special case where $\omega_3 = \alpha\omega_1 + \beta\omega_2$ and $\mathbf{k}_3 = \alpha\mathbf{k}_1 + \beta\mathbf{k}_2$ can one still boost to a time-independent wave-frame. Hence, the extension of the present problem to three or more co-planer waves is, in general, fundamentally different in character from the two-wave problem investigated in this work. The additional "half degree" of freedom, not removable through coordinate transformation, opens up the possibility of Arnold diffusion[12,13], not generally present in two-degree-of-freedom, autonomous systems.

Upon substituting the expressions for the fields, given by Eqs. (1)–(3), into Eqs. (4) and (5), one obtains the following equations of motion for the guiding-center orbits:

$$\frac{dv_{\|}}{dt} = -\frac{e}{m_e}\sum_{i=1,2}\phi_i k_{i_{\|}}(x)\sin(\mathbf{k}_i \cdot \mathbf{r}) \tag{6}$$

$$\frac{dx}{dt} = \frac{c}{B_0} \sum_{i=1,2} \phi_i k_{i_\perp}(x) \sin(\mathbf{k}_i \cdot \mathbf{r}) \tag{7}$$

$$\frac{dy}{dt} = v_\parallel \sin\frac{x}{L_s} - w_\perp(x) \cos\frac{x}{L_s} \tag{8}$$

$$\frac{dz}{dt} = v_\parallel \cos\frac{x}{L_s} + w_\perp(x) \sin\frac{x}{L_s}, \tag{9}$$

where

$$w_\perp(x) \equiv w_y \cos\frac{x}{L_s} - w_z \sin\frac{x}{L_s}$$

$$k_{i_\perp}(x) \equiv k_{i_y} \cos\frac{x}{L_s} - k_{i_z} \sin\frac{x}{L_s}$$

$$k_{i_\parallel}(x) \equiv k_{i_y} \sin\frac{x}{L_s} + k_{i_z} \cos\frac{x}{L_s}.$$

For notational convenience, we have dropped the primes denoting wave-frame quantities. Here, and in the remainder of the discussion, the phase space coordinates are understood to refer to wave-frame quantities. In comparing these equations with earlier investigations of motion in one wave, one should bear in mind that other authors[14] have expressed the motion in terms of a parallel velocity relative to the *lab* frame and a phase coordinate, $\theta = \mathbf{k} \cdot \mathbf{r} - \omega t$, relative to the *wave* frame; a sort of mixed representation. Our coordinates are the particle's physical position and velocity as seen by an observer in an inertial frame moving with the waves.

The helical symmetry of the $\mathbf{B}$ field specified in Eq. (1) permits one, without loss of generality, to take $k_{1_z} = 0$. One may choose the y-axis of the coordinate system to be parallel to $\mathbf{k}_1$. Then one specifies the origin of the x-axis as the point at which $\mathbf{B}$ is orthogonal to $\mathbf{k}_1$ to recover the expression for $\mathbf{B}$ given in Eq. (1).

One may verify, by differentiation, that the energy function,

$$H \equiv \frac{1}{2} m_e v_\parallel^2 - e\Phi'(x, y, z), \tag{10}$$

is conserved under the motion specified by Eqs. (6)–(9). Here, Φ', the electrostatic potential in the wave-frame, is given by

$$\Phi' \equiv \sum_{i=1,2} \phi_i \cos \mathbf{k}_i \cdot \mathbf{r} - \frac{1}{c}\mathbf{w} \cdot \mathbf{A}(\mathbf{x}), \tag{11}$$

where $\mathbf{A}$ is a vector potential consistent with $\mathbf{B} = \nabla \times \mathbf{A}$. For the magnetic field of Eq. (1), $\mathbf{A}$ may be taken as

$$\mathbf{A} \equiv B_0 L_s \left[\hat{\mathbf{e}}_y \sin \frac{x}{L_s} + \hat{\mathbf{e}}_z \cos \frac{x}{L_s} \right]. \tag{12}$$

A. The Hamiltonian Equations: Non-Canonical and Canonical Coordinates

The equations of motion (4)–(5) have the virtue of clearly displaying the principle physics of the present problem: namely, that the electric field produces acceleration along the field lines and $\mathbf{E} \times \mathbf{B}$ drifts across the field lines. This reduced set of equations, however, suffers the drawback of not retaining the underlying Hamiltonian structure of the complete Newton-Lorentz equations of motion. Littlejohn [15] corrects this deficiency of the simple drift equations by systematically constructing the guiding-center equations, to arbitrary order in the magnetic moment. Following his phase space Lagrangian formulation of guiding-center motion [14], the equations of motion, to lowest order in the magnetic moment, may be obtained by applying Hamilton's principal to the Lagrangian

$$L(v_\parallel, x, y, z) = \frac{d\mathbf{r}}{dt} \cdot \left[m_e v_\parallel \hat{\mathbf{b}} - \frac{e}{c}\mathbf{A} \right] - H, \tag{13}$$

where the Hamiltonian function, H, and the vector-potential, $\mathbf{A}$, are defined by Eqs. (10)–(12). One is to regard the four phase space coordinates, $v_\parallel$, x, y, and z, as the generalized coordinates.

Defining the 4-component vectors $\mathbf{z} \equiv (v_\parallel, \mathbf{r})$ and $\mathbf{P}(\mathbf{z}) \equiv (0, m_e v_\parallel \hat{\mathbf{b}} - (e/c)\mathbf{A})$, and using the Einstein summation convention, the Lagrangian (13) may be rewritten as

$$L(\mathbf{z}, \dot{\mathbf{z}}) = \dot{\mathbf{z}}^i P_i(\mathbf{z}) - H(\mathbf{z}). \tag{14}$$

The only non-vanishing components of $\mathbf{P}$ are

$$P_y(v_\parallel, x) \equiv m_e(v_\parallel - \omega_{ce}L_s)\sin\frac{x}{L_s} \tag{15}$$

$$P_z(v_\parallel, x) \equiv m_e(v_\parallel - \omega_{ce}L_s)\cos\frac{x}{L_s}. \tag{16}$$

Independent variation of the z^i leads to the Euler-Lagrange equations $\omega_{ij}\dot{z}^j = \partial H/\partial z^i$, where the symplectic tensor $\boldsymbol{\omega}$ is defined as $\omega_{ij} \equiv \partial P_j/\partial z^i - \partial P_i/\partial z^j$. The equations of motion, for the non-canonical coordinates z^i, are then given by

$$\frac{dz^i}{dt} = J^{ij}\frac{\partial H}{\partial z^j}, \tag{17}$$

where the cosymplectic tensor $\mathbf{j}$ is defined to be the inverse of $\boldsymbol{\omega}$. $\mathbf{j}$ may be written in terms of the block matrix $\mathbf{M}$ and its transpose $\mathbf{M}^T$ as

$$\mathbf{j} \equiv \begin{pmatrix} 0 & \mathbf{M} \\ -\mathbf{M}^T & 0 \end{pmatrix},$$

where

$$\mathbf{M} \equiv \frac{1}{m_e}\begin{pmatrix} -\sin\frac{x}{L_s} & -\cos\frac{x}{L_s} \\ \frac{1}{\omega_{ce}\beta}\cos\frac{x}{L_s} & -\frac{1}{\omega_{ce}\beta}\sin\frac{x}{L_s} \end{pmatrix}.$$

Here, the function β, derived by Littlejohn, is defined as

$$\beta \equiv 1 + \frac{v_\parallel}{\omega_{ce}}\hat{\mathbf{b}}\cdot\nabla\times\hat{\mathbf{b}} = 1 - \frac{m_e c v_\parallel}{eB_0L_s},$$

and arises from the twisting of the magnetic field lines due to the sheared $\mathbf{B}(x)$. The term $\frac{m_e c v_\parallel}{eB_0L_s}$ in β equals $\frac{\rho_L v_\parallel}{L_s v_\perp}$, where ρ_L is the Larmor radius. Assuming $v_\perp \simeq v_\parallel$ and $\rho_L \ll L_s$, this term is small, and $\beta \simeq 1$. With β approximated by unity, Eq. (17) becomes identical to Eqs. (6)–(9).

The conservation of energy is readily apparent in the Hamiltonian formulation. The total time-derivative of H may be written $dH/dt = (\partial H/\partial z^i)J^{ij}(\partial H/\partial z^j)$. From the

antisymmetry of J, one immediately sees that H is a constant of the motion. If, additionally, ϕ_2 is taken to be zero, the Lagrangian (14) becomes cyclic in the coordinate z. Thus, with only one wave, the z-component of the gyro-phase-averaged canonical momentum, P_z, is a conserved quantity.

From the definition of ω_{ij}, one finds that the Jacobi tensor, $\mathbf{S}$, whose covariant components are defined by

$$S_{lmn} \equiv \frac{\partial \omega_{lm}}{\partial z^n} + \frac{\partial \omega_{mn}}{\partial z^l} + \frac{\partial \omega_{nl}}{\partial z^m},$$

is identically zero. According to Darboux's theorem, any antisymmetric, non-singular $\mathbf{j}$ with vanishing Jacobi tensor, may be brought into canonical form by a suitable coordinate transformation. (We note that setting $\beta = 1$ in $\mathbf{j}$ yields a Jacobi tensor, $\mathbf{S}$, which ceases to vanish, thus demonstrating that Eqs. (6)–(9) are non-Hamiltonian.) Darboux's theorem offers no clue for finding such a transformation. However, an appropriate transformation for the present system is obvious from the form of the Lagrangian:

$$L = \dot{y} P_y(v_\parallel, x) + \dot{z} P_z(v_\parallel, x) - H(v_\parallel, x, y, z).$$

Using P_y and P_z as generalized coordinates, in lieu of $v_\parallel$ and x, the Lagrangian becomes $L = \dot{y}P_y + \dot{z}P_z - H(P_y, P_z, y, z)$. The Euler-Lagrange equations which result by considering P_y, P_z, y and z as independent coordinates have the form of Hamilton's equations [15]:

$$\begin{aligned} \dot{y} &= \frac{\partial H}{\partial P_y} \qquad & \dot{P}_y &= -\frac{\partial H}{\partial y} \\ \dot{z} &= \frac{\partial H}{\partial P_z} \qquad & \dot{P}_z &= -\partial H \, or \, \partial z. \end{aligned} \tag{18}$$

The Hamiltonian (10) must be rewritten in terms of P_y, P_z, y and z by inverting Eqs. (15)–(16) to express $v_\parallel$ and x in terms of P_y and P_z. One obtains

$$H = \frac{1}{2m_e}\left[\frac{eB_0L_s}{c} + \sigma\sqrt{P_y^2 + P_z^2}\right]^2 + \sigma\frac{eB_0L_s[w_yP_y + w_zP_z]}{c\sqrt{P_y^2 + P_z^2}} - e\sum_{i=1,2}\phi_i\cos(\mathbf{k}_i\cdot\mathbf{r}), \tag{19}$$

where $\sigma \equiv \pm 1$. The Hamiltonian has two branches, specified by σ, since $v_{\|}$ and x are multi-valued functions of P_y and P_z. Darboux's theorem is local. It doesn't guarantee a global set of canonical coordinates. It is, however, likely that orbits of interest will not cross from one branch to the other. To do so requires that $P_y^2 + P_z^2$ go to zero. From Eqs. (15) and (16), one finds that this, in turn, requires $v_{\|}$ to go through $L_s v_\perp / \rho_L$, which is a large number.

B. Dimensionless Units

The particle motion, given by either Eqs. (6)–(9), Eq. (17), or Eqs. (18), depends upon a fairly large set of dimensioned parameters:

$$\{e, m_e, c, \phi_1, \phi_2, k_{1_y}, k_{2_y}, k_{2_z}, B_0, L_s, \omega_1, \omega_2\}.$$

By exploiting dynamical similarity, one can reduce the number of free parameters from 12 to 5. This is accomplished by expressing the equations of motion in terms of a set of dimensionless variables. We now outline the approach we have taken in arriving at a suitable parametrization.

We first establish a relevent scale-length for the x-coordinate. Consider the simplified problem of motion in one wave, in the limit $\mathbf{w} \longrightarrow 0$ (i.e., the wave is stationary in the lab frame). Furthermore, assume that excursions in x away from the rational surface ($x = 0$) remain small compared with the shear length, L_s. The two conserved quantities, $P_z \approx m_e v_{\|} + \frac{\omega_{ce} m}{L_s} \frac{x^2}{2}$ and $H \equiv \frac{1}{2} m_e v_{\|}^2 - e\phi_1 \cos(k_{1_y} y)$, may be combined to express the projection of the orbits upon the x-y plane. We discuss the form of these orbits in more detail in Sec. III. For the present, we use the result that the motion remains bounded in the x-direction, and that the maximum excursion in the x-direction is attained by a homoclinic orbit parametrized by $H = e\phi_1$, $P_z = 2 m_e v_0$, where

$$v_0 \equiv \sqrt{e\phi_1 / m_e}$$

is the familiar trapping velocity. This orbit, which is pictured in Fig. 1a, has turning points at $x = \pm\sqrt{8L_s v_0/\omega_{ce}}$. This maximal excursion distance suggests defining the dimensionless coordinate

$$\tilde{x} \equiv \frac{x}{\epsilon L_s},$$

where

$$\epsilon \equiv \sqrt{\frac{v_0}{\omega_{ce} L_s}}.$$

Substituting this into the expression for the canonical momentum, one obtains $\frac{P_z}{m_e v_0} = v_\parallel/v_0 + \tilde{x}^2/2 \equiv \tilde{P}_z$. We therefore define the rescaled parallel velocity

$$u \equiv \frac{v_\parallel}{v_0}.$$

For $x \ll L_s$ and $\phi_2 = 0$, Eq. (7) becomes $d\tilde{x}/dt = k_{1_y} v_0 \epsilon \sin(\mathbf{k}_1 \cdot \mathbf{r})$. We therefore define the dimensionless time

$$\tilde{t} \equiv k_{1_y} v_0 \epsilon t.$$

It is convenient to replace the coordinates y and z with the two phase coodinates

$$\psi_i \equiv \mathbf{k}_i \cdot \mathbf{r}, \qquad i = 1, 2.$$

Using the $\beta = 1$ approximation, Eqs. (6)–(9), we obtain the following equations of motion:

$$\frac{du}{d\tilde{t}} = -\frac{1}{\epsilon}\{\sin(\epsilon\tilde{x})\ \sin\psi_1 + \phi k\ \sin(\epsilon\tilde{x} + \theta)\ \sin\psi_2\} \tag{20}$$

$$\frac{d\tilde{x}}{d\tilde{t}} = \cos(\epsilon\tilde{x})\ \sin\psi_1 + \phi k\ \cos(\epsilon\tilde{x} + \theta)\ \sin\psi_2 \tag{21}$$

$$\frac{d\psi_1}{d\tilde{t}} = \frac{1}{\epsilon}\{u\ \sin(\epsilon\tilde{x}) - [\tilde{w}_y \cos(\epsilon\tilde{x}) - \tilde{w}_z \sin(\epsilon\tilde{x})]\cos(\epsilon\tilde{x})\} \tag{22}$$

$$\frac{d\psi_2}{d\tilde{t}} = \frac{k}{\epsilon}\{u\ \sin(\epsilon\tilde{x} + \theta) - [\tilde{w}_y \cos(\epsilon\tilde{x}) - \tilde{w}_z \sin(\epsilon\tilde{x})]\cos(\epsilon\tilde{x} + \theta)\}, \tag{23}$$

where $k \equiv \mid \mathbf{k}_2 \mid / \mid \mathbf{k}_1 \mid$, $\phi \equiv \phi_2/\phi_1$, $\tilde{\mathbf{w}} \equiv \mathbf{w}/v_0$, and θ is the angle between the wave-vectors.

We assume that the separation, $\Delta x \equiv \theta L_s$, between the mode-rational surfaces associated with the two waves is small compared with the shear length L_s. We also assume that the radial excursion, $x \equiv \epsilon L_s \tilde{x}$, of the particle away from the first wave's rational surface remains small compared with the shear length. We therefore make the approximations $\epsilon\tilde{x} \ll 1$ and $\theta \ll 1$ and Eqs. (20)–(23) become

$$\frac{du}{d\tilde{t}} = -\left[\tilde{x}\ \sin\psi_1 + \phi k(\tilde{x} + \theta/\epsilon)\sin\psi_2\right] \tag{24}$$

$$\frac{d\tilde{x}}{d\tilde{t}} = \sin\psi_1 + \phi k\ \sin\psi_2 \tag{25}$$

$$\frac{d\psi_1}{d\tilde{t}} = u\tilde{x} + \tilde{w}_z\tilde{x} - \frac{\tilde{w}_y}{\epsilon} \tag{26}$$

$$\frac{d\psi_2}{d\tilde{t}} = k\left[u\left(\tilde{x} + \frac{\theta}{\epsilon}\right) + \tilde{w}_z\tilde{x} - \frac{\tilde{w}_y}{\epsilon}\right]. \tag{27}$$

Thus, a set of 5 parameters, $\{\tilde{w}_y/\epsilon, \phi, k, \theta/\epsilon, \tilde{w}_z\}$, is required to specify the two-wave system. We note that the system of equations (24)–(27) is Hamiltonian. We have found that they can be written in the form $\dot{z}^i = J^{ij}\partial H/\partial z^j$, where J is an antisymmetric, non-singular tensor, with vanishing Jacobi tensor S. The Hamiltonian structure which was lost in making the $\beta = 1$ approximation was apparently regained fortuitously upon making the further approximations $\epsilon\tilde{x} \ll 1$, $\theta \ll 1$.

C. The Constant Parallel Velocity Approximation

If the magnitude of $v_\parallel$ is large, one sees, from the invariance of the Hamiltonian, Eq. (10), that the relative variation in $v_\parallel$ becomes small. Thus, in the limit of large energy, u may be treated as a constant. Eqs. (26) and (27) may then be combined to give $\frac{d}{d\tilde{t}}(k\psi_1 - \psi_2) = -uk\theta/\epsilon$. Solving for ψ_2, one finds $\psi_2 = k\psi_1 + uk\theta(\tilde{t} - \tilde{t}_0)/\epsilon$, where $\tilde{t}_0$ is determined by initial conditions. Substituting this into Eq. (25), one finds that Eqs. (25)–(26) assume the form of a non-autonomous, canonical system, generated by the

Hamiltonian

$$\eta(\psi_1,\tilde{x},\tilde{t}) = \frac{1}{2}(u+\tilde{w}_z)\left[\tilde{x} - \frac{\tilde{w}_y}{\epsilon(u+\tilde{w}_z)}\right]^2 + \cos\psi_1 + \phi\cos[k\psi_1 + uk\theta(\tilde{t}-\tilde{t}_0)/\epsilon] \qquad (28)$$

in which ψ_1 and $\tilde{x}$ fill the role of canonical coordinate and momentum, respectively. We emphasize that the Hamiltonian $\eta(\psi_1,\tilde{x},\tilde{t})$, valid only for large $v_{\|}$, is distinct from the generally applicable Hamiltonian treatment presented in Sec. IIa. of this work. Combining Eqs. (25) and (26), one obtains the following second order equation for ψ_1 :

$$\frac{d^2\psi_1}{d\tilde{t}^2} = (u+\tilde{w}_z)\left[\sin\psi_1 + \phi k\sin\left(k\psi_1 + uk\theta(\tilde{t}-\tilde{t}_0)/\epsilon\right)\right]. \qquad (29)$$

In the limit of large parallel velocity ($u \gg 1$), the problem thus reduces to the familiar perturbed pendulum, which has been studied extensively in the literature.[8,16]

To motivate our consideration of the regime where the constant $v_{\|}$ approximation ceases to be valid, consider a particle with $u = 0$. The parallel velocity in the lab-frame is then $v_{\|_{lab}} = \mathbf{w}\cdot\hat{\mathbf{b}}$. If the particle is located at a value of x where $\hat{\mathbf{b}}$ is parallel to $\mathbf{w}$, then $\mathbf{k}_i\cdot\hat{\mathbf{b}}v_{\|_{lab}} = \mathbf{k}_i\cdot\hat{\mathbf{b}}\mathbf{w} = \mathbf{k}_i\cdot\mathbf{w} \equiv \omega_i$, for $i = 1,2$. Hence, such a particle is simultaneously Landau resonant with both waves. The simultaneous resonance of electrons with two plane waves leads to the anomalously large nonlinear Vlasov-Poisson mode-coupling matrix elements, analyzed by Choi and Horton [18] from third order perturbation theory. Here, these orbits are calculated exactly.

D. Poincaré Surfaces of Section

The conservation of H confines a given orbit to a 3-dimensional manifold in phase space. When only one wave is present, a second conserved integral, P_z, exists and the motion is constrained to lie on a 2-dimensional manifold. We treat ϕ, the ratio of wave amplitudes, as a perturbation parameter. For $\phi \neq 0$, a second isolating integral of motion may cease to exist in some regions of phase space, leading to the stochastic instability.

Each constant-H surface is of the same generic variety as the magnetic field line problem in fusion confinement devices with toroidal geometry. It may therefore be of some help in visualizing the nature of this system to recast it in the language of tokamak physics. To make the correspondence concrete, consider Eqs. (24)–(27). The conserved integral for these equations is

$$H = u^2/2 - \cos\psi_1 - \phi\cos\psi_2 + \tilde{w}_y\tilde{x}/\epsilon - \tilde{w}_z\tilde{x}^2/2. \tag{30}$$

Let us define the strictly positive quantity $\rho \equiv \exp(u + \tilde{x}^2/2)$. The time-derivative of ρ is $\dot{\rho} = -\phi k\theta\epsilon^{-1}\rho\sin\psi_2$. One can invert ρ and H to express $\dot{\psi}_1$ and $\dot{\psi}_2$ as functions of H, ρ, ψ_1 and ψ_2 (and branch parameters). Thus adopting the coordinates (ρ, ψ_1, ψ_2), with H fixed, one sees that ρ is analogous to the minor radius of the tokamak, and ψ_1 and ψ_2 correspond to the poloidal and toroidal angles, as illustrated in Fig. 2. When $\phi = 0$, $\dot{\rho} = 0$ and the orbits are confined to nested toroidal surfaces of circular cross-section. For $\phi \neq 0$, one sees the emergence of islands, as shown in the figure, and, for large enough perturbations, the destruction of "good" two-dimensional surfaces. Unlike the tokamak field problem, we must contend with a continuous class of such toroidal systems; one "tokamak" for each value of H.

We use the method of Poincaré surfaces of section to observe, in numerical experiments, the destruction of the second isolating integral. For a given value of H, we integrate a number of orbits, plotting a point in the $(\psi_1 \bmod 2\pi, \tilde{x})$-plane each time the trajectory passes through the surface $\psi_2 = 0 \mod 2\pi$. (Since u is a double-valued function of H, $\tilde{x}$, ψ_1 and ψ_2, only those orbits crossing the surface of section with a given sign of u should be plotted, so as to avoid a "double-exposure" effect.) Orbits for which a second isolating integral is preserved produce points in the Poincaré map which fall on one-dimensional curves. Orbits for which the second integral is destroyed yield a haphazard scatter of

points, filling an area. Examples of Poincaré surfaces of section are given in Figs. 3–5 which we discuss below.

The Poincaré map defined above is a measure-preserving map of the $(\psi_1, \tilde{x})$-plane onto itself. One can show that the quantity

$$\delta A \frac{\dot{\psi}_2}{\frac{\partial H}{\partial u}} \exp\left[-\int^{\tilde{t}} d\tilde{t} \frac{\partial \dot{z}_i}{\partial z_i}\right]$$

remains invariant under the above defined Poincaré map, where δA is an infinitesimal area element in the surface of section, and $\partial \dot{z}_i / \partial z_i$ is the divergence of the flow velocity. For Eqs. (20)–(23), the divergence of the flow velocity is $\partial \dot{\tilde{x}} / \partial \tilde{x} = \epsilon^2 du/d\tilde{t}$, hence $\delta A \dot{\psi}_2 e^{-\epsilon^2 u}/u$ is invariant under the Poincaré map. For Eqs. (24)–(27), the flow in the 4-dimensional phase space is incompressible, and $\delta A \dot{\psi}_2 / u$ is invariant under the Poincaré map.

III. Motion in One Wave — The Unperturbed Problem

Before discussing the two-wave problem, we give the properties of the unperturbed problem. With $\phi = 0$ (one wave), the equations of motion (24)–(26) reduce to the one parameter family of trajectories

$$\dot{\tilde{u}} = -\tilde{x} \sin \psi_1 \tag{31}$$

$$\dot{\tilde{x}} = \sin \psi_1 \tag{32}$$

$$\dot{\psi}_1 = \tilde{u}\tilde{x} - \lambda, \tag{33}$$

where $\lambda \equiv \tilde{w}_y / \epsilon$. The parameter $\tilde{w}_z$ has been absorbed into the parallel velocity by defining a "shifted" velocity $\tilde{u} \equiv u + \tilde{w}_z$. The motion is completely specified, within a similarity transformation, by the initial coordinate values and the single parameter λ.

One can verify that the quantities $\tilde{H} = \tilde{u}^2/2 - \cos\psi_1 + \lambda\tilde{x}$ and $\tilde{P}_z = \tilde{u} + \tilde{x}^2/2$ are invariants of the motion. $\tilde{H}$ and $\tilde{P}_z$ are related to the small x/L_s limit versions of Eqs. (10)

and (16) by $\tilde{P}_z \equiv P_z/(m_e v_0)$ and $\tilde{H} \equiv (H + w_z P_z)/(m v_0^2)$. The system of equations (31)–(33) is integrable, in the sense that expressions for the motion may be reduced to quadrature. However, the prospect of obtaining general solutions for the motion in terms of well-known analytic functions seems doubtful. The two constants of the motion may be combined with Eq. (31) to give

$$d\tilde{t} = \frac{d\tilde{u}}{-\sigma_1\sigma_2\sqrt{2[\tilde{P}_z - \tilde{u}]}\sqrt{1 - \left\{\tilde{u}^2/2 - \tilde{H} + \lambda\sigma_1\sqrt{2[\tilde{P}_z - \tilde{u}]}\right\}^2}}, \tag{34}$$

where σ_1 and σ_2 are branch parameters equal to ± 1. Even for the case $\lambda = 0$, the expression under the radical is a quintic polynomial in $\tilde{u}$. This apparently precludes the possibility of integrating Eq. (34) in terms of elliptic integrals, except for special values of $\tilde{H}$ and $\tilde{P}_z$ where singular points in the expression for $d\tilde{t}/d\tilde{u}$ degenerate into simple poles (i.e. homoclinic orbits).

We now undertake a classification of the various orbits which are possible in one wave. Using the two integrals $\tilde{H}$ and $\tilde{P}_z$ of the motion, the projections of the orbits upon the $(\psi_1, \tilde{x})$-plane are given by

$$\tilde{H} = \frac{1}{2}\left[\tilde{P}_z - \frac{\tilde{x}^2}{2}\right]^2 - \cos\psi_1 + \lambda\tilde{x}. \tag{35}$$

Each orbit in the $(\psi_1, \tilde{x})$-plane is specified by the values of $\tilde{H}$ and $\tilde{P}_z$. For the purpose of graphically illustrating the various kinds of orbits which may occur, we fix the value of $\tilde{P}_z$ and plot a number of orbits in the $(\psi_1, \tilde{x})$-plane for several values of $\tilde{H}$. One's first instinct might be to take the opposite tack and fix the value of $\tilde{H}$, constructing a plot of several orbits having various values of $\tilde{P}_z$. Plotting orbits on the constant-$\tilde{H}$ surface seems the preferable approach, since $\tilde{H}$ remains a good constant of the motion when we go to the two-wave problem; whereas $\tilde{P}_z$ does not. However, since $\tilde{u}$ is a double-valued function of

$\tilde{H}$, it is possible for two distinct trajectories to cross in the constant-$\tilde{H}$ projection. This complication does not arise if we consider orbits plotted in the constant-$\tilde{P}_z$ projection; we have taken this approach in order to render a comprehensive orbit classification tractable. Eliminating $\tilde{u}$ in favor of $\tilde{P}_z$, Eqs. (32)–(33) become

$$\dot{\tilde{x}} = \sin\psi_1 \qquad\qquad \dot{\psi}_1 = \left[\tilde{P}_z - \frac{\tilde{x}^2}{2}\right]\tilde{x} - \lambda. \tag{36}$$

Treating ψ_1 and $\tilde{x}$ as canonical coordinates, Eq. (35) is the Hamiltonian which generates the equations of motion (36).

The phase portraits in the $(\psi_1, \tilde{x})$-plane, produced by Eqs. (36), fall into twelve distinct categories, depending upon the values of $\tilde{P}_z$ and λ. Figs. 1a–1l are representative of the possible classes. Figs. 1b–1f are all topologically equivalent to the pendulum. Fig. 6 gives an atlas showing which of the classes *a* through *l* occurs for each value of the parameter pair $\tilde{P}_z$ and λ. For example, each pair of parameters $(\lambda, \tilde{P}_z)$ falling within the two-dimensional domain labeled *g* in Fig. 6 will give rise to a phase portrait which is topologically similar to the orbits of Fig. 2g. The classes *c, d, h, i* and *l* are one-dimensional sets in the $(\lambda, \tilde{P}_z)$-plane, while the classes *a, e* and *f* are zero-dimensional sets. In order to construct such an atlas, we carry out a singular point analysis of Eqs. (36).

A. Orbit Classes for $\lambda \neq 0$

Let us first consider the case $\lambda \neq 0$. One may assume, without loss of generality, that λ is positive, since the one-wave equations of motion (31)–(33) remain invariant under the transformation $(\tilde{x}, \psi_1, \lambda) \longrightarrow (-\tilde{x}, -\psi_1, -\lambda)$. Looking for the fixed points of Eqs. (36), defined by $\dot{\psi}_1 = \dot{\tilde{x}} = 0$, one finds that the fixed points occur for $\psi_1 = n\pi$, n an integer, and $\tilde{x} = \lambda^{1/3}\zeta$, where ζ is a root of the cubic equation

$$b = (\zeta^2 + 2\zeta^{-1})/3 \tag{37}$$

and b is defined by the equation

$$\tilde{P}_z = \frac{3}{2}\lambda^{2/3} b. \tag{38}$$

Eq. (37) is plotted in Fig. 7, showing b as a function of ζ. Looking at this plot, one sees that, for $b < 1$, only one real root, which we call ζ_3, exists. It is always negative. For $b > 1$, three real roots to Eq. (37) exist. One can express these roots as

$$\zeta_1 = 2\sqrt{b}\cos\left[\frac{1}{3}\arccos\left(-b^{-3/2}\right)\right] \tag{39}$$

$$\zeta_2 = 2\sqrt{b}\cos\left[\frac{4\pi}{3} + \frac{1}{3}\arccos\left(-b^{-3/2}\right)\right] \tag{40}$$

$$\zeta_3 = 2\sqrt{b}\cos\left[\frac{2\pi}{3} + \frac{1}{3}\arccos\left(-b^{-3/2}\right)\right], \quad (b > 1) \tag{41}$$

$$= -\sqrt[3]{1-\sqrt{1-b^3}} - \sqrt[3]{1+\sqrt{1-b^3}}, \quad (b \leq 1)$$

where $\zeta_1 > 1$, $0 < \zeta_2 < 1$, and $\zeta_3 < 0$.

A stability analysis of Eqs. (36) indicates that the point $(\psi_1, \tilde{x}) = (n\pi, \lambda^{1/3}\zeta)$ is a stable fixed point if $(-1)^n[\zeta^{-1} - \zeta^2] < 0$, and unstable otherwise. From this relation, one can determine the stability of the fixed points corresponding to the three roots for ζ and even and odd values of n. These results are summarized in Table I.

In Fig. 6, the bottom curve is the function $\tilde{P}_z = \frac{3}{2}\lambda^{2/3}$, which, according to Eq. (38), corresponds to $b = 1$. This curve thus divides the $(\lambda, \tilde{P}_z)$-plane into the 1-root and 3-root regions. Below this curve, the plots are all topologically similar to the pendulum, e.g. Fig. 1b.

When $b = 1$, the topology is also that of the pendulum. However, the coalescence of the two roots ζ_1 and ζ_2 results in the appearence of cusp singularities at $\tilde{x} = \lambda^{1/3}$. When $\lambda > (16/27)^{3/4}$, the cusps corresponding to both n odd and n even fall outside the separatrix, as illustrated in Fig. 1c. For $\lambda < (16/27)^{3/4}$, one set of cusps falls inside the

separatrix, as illustrated in Fig. 1d. For $\lambda = (16/27)^{3/4}$, one set of cusps occur on the separatrix (Fig. 1e).

For $b > 1$ and $\lambda \neq 0$, five classes are possible. These are illustrated in Figs. 1g–1k. Writing Eq. (35) in terms of b and ζ,

$$\tilde{H}\lambda^{-4/3} = \frac{1}{8}\left[3b - \zeta^2\right]^2 - \lambda^{-4/3}\cos\psi_1 + \zeta. \tag{42}$$

For the class of orbits illustrated in Fig. 1h, the X-points at $(\pi, \lambda^{1/3}\zeta_1)$ and $(0, \lambda^{1/3}\zeta_2)$ fall on the same trajectory. Hence, they share a common value of $\tilde{H}$. Using Eq. (42), one finds that the plots of class e must obey the relation

$$\lambda = 8\left[\zeta_2^4 - \zeta_1^4 - 6b(\zeta_2^2 - \zeta_1^2) + 8(\zeta_2 - \zeta_1)\right]^{-3/4}. \tag{43}$$

Eqs. (43) and (38), along with the definitions of ζ_1, ζ_2, and ζ_3 given in Eqs. (39)–(41), constitute a parametric representation of a curve in the $(\lambda, \tilde{P}_z)$-plane, where the parameter b is allowed to range from 1 to ∞. This yields the curve labeled h in Fig. 6.

Similarly, the class of orbits illustrated in Fig. 1i, where the X-points at $(0, \lambda^{1/3}\zeta_2)$ and $(\pi, \lambda^{1/3}\zeta_3)$ fall on the same trajectory, occur for values of $\tilde{P}_z$ and λ obeying the parametric relationship given by Eq. (38) and

$$\lambda = 8\left[\zeta_2^4 - \zeta_3^4 - 6b(\zeta_2^2 - \zeta_3^2) + 8(\zeta_2 - \zeta_3)\right]^{-3/4}. \tag{44}$$

This curve is labeled i in Fig. 6. After finding the above classes of zero measure in the $(\lambda, \tilde{P}_z)$-plane, as well as those discussed in Sec. IIIb., it is a straightforward matter to assign the remaining classes of non-zero measure, g, j and k, to the appropriate regions of the atlas.

B. Orbit Classes for $\lambda = 0$

We now discuss the orbits for the case where the wave is stationary in the lab frame. This regime is represented by the $\tilde{P}_z$-axis in Fig. 6. For $\lambda = 0$, the fixed points are given by $\psi_1 = n\pi$ and $\tilde{x}$ equal to 0, as well as $\pm\sqrt{2\tilde{P}_z}$ when $\tilde{P}_z$ is positive. For $\tilde{P}_z < 0$, the plots are topologically similar to those of the pendulum, belonging to the class b discussed for the $\lambda \neq 0$ case. However, for $\lambda = 0$, the orbits are symmetric about the ψ_1 axis. When $\tilde{P}_z = 0$, the triply degenerate root for $\tilde{x}$ leads to a separatrix which is parabolic-shaped, rather than linear, at the unstable singularities, and motion near the stable fixed points which is an harmonic. This case is illustrated in Fig. 1f.

As $\tilde{P}_z$ becomes positive, the fixed points bifurcate into a triplet of fixed points. Since, for $\lambda = 0$, $\tilde{H}$ is an even function of $\tilde{x}$, the fixed points at $(\psi_1, \tilde{x}) = (n\pi, \pm\sqrt{2\tilde{P}_z})$, n odd, all have the same value of $\tilde{H}$; namely $\tilde{H} = 1$. For $0 < \tilde{P}_z \leq 2$, these X-points all fall on the same trajectory. This class of orbits is illustrated in Fig. 1l. As $\tilde{P}_z$ is increased to 2, one sees, from Eq. (35) that the figure-eight separatrix of Fig. 1l also attains a value of $\tilde{H}$ equal to 1. All of the separatrices merge into one web for $\tilde{P}_z = 2$, $\lambda = 0$, resulting in the orbits shown in Fig. 1a.

As $\tilde{P}_z$ is made greater than 2, a reconnection of the separatrices occurs, producing the topology of Fig. 1k. As with class b, the class k occurs for both $\lambda \neq 0$ and $\lambda = 0$. Again, in the latter case, the orbits differ from those of Fig. 1k in that they are symmetric about the ψ_1 axis. A set of 3 pendulum-like "islands" emerge. The upper and lower islands wander off to $\pm\infty$ as $\tilde{P}_z$ is made large. The stable fixed points at the centers of these islands simply represent particles with zero parallel velocity, sitting at the bottom of the electrostatic potential well. Such particles feel a stable restoring force along the field lines for any value of $\tilde{x} \neq 0$.

Setting $\lambda = 0$ in Eq. (35) and using our knowledge of where the X-points occur, we can find a set of relatons between $\tilde{P}_z$ and $\tilde{H}$ which hold on the separatrices. For the separatrix labeled α in Fig. 1b, one finds $\tilde{H} = \tilde{P}_z^2/2+1$. For the separatrices labeled ε and γ in Figs. 1k and 1l, $\tilde{H} = \tilde{P}_z^2/2 - 1$. All of the separatrices μ, β, κ and δ have a constant value of $\tilde{H} = 1$. These relations are plotted in Fig. 8. The curves in Fig. 8 thus constitute a locus of the separatrices for the $\lambda = 0$ case. Each point in the $(\tilde{P}_z, \tilde{H})$-plane of Fig. 8 represents an orbit, and due to the constancy of $\tilde{P}_z$ and $\tilde{H}$ for one wave, a point remains stationary with time in this projection. This plot suppresses the phase information. Those points falling on one of the plotted curves are orbits of infinite period.

IV. Motion in Two Waves

We now consider the perturbed problem. For $\phi \neq 0$, one sees the emergence of resonance "islands," as shown in Fig. 2. These islands are located near the tori of the unperturbed problem with rational winding numbers. As the perturbation strength ϕ is increased, the islands grow in size. One sees a transition to stochastic behavior as islands associated with neighboring, low-order rational surfaces approach each other. In subsection A, we calculate island overlap criteria by approximating the locations and widths of the lowest order resonance islands, using perturbation theory. In subsection B, we obtain global stochasticity criteria by investigating the conditions for strong interaction of the primary trapping regions associated with each of the two waves.

In these analyses we confine the discussion to the case $\mathrm{w} = 0$. We have focused our attention upon this limiting case, in an attempt to simplify the problem. We should, however, point out that some qualitative changes in the problem occur for finite values of w. One striking difference is the emergence of a broken symmetry due to the electric current in the z-direction, which is responsible for the shear in the magnetic field. The

sign of j_z fixes a "preferred" direction. The mobility of the electrons in the x-direction depends upon whether the z-component of the wave-frame's velocity is parallel or anti-parallel to this current. The potential energy, as seen in the wave-frame, has an extremum with respect to the x-coordinate at $\tilde{x} = \tilde{w}_y/(\epsilon\tilde{w}_z)$. This extremum is either a maximum or a minimum, depending on whether $\tilde{w}_z$ is positive or negative.

For $\tilde{w}_z > 0$, the conserved Hamiltonian $H = u^2/2 - \cos\psi_1 - \phi\cos\psi_2 + \tilde{w}_y\tilde{x}/\epsilon - \tilde{w}_z\tilde{x}^2/2$ imposes no constraint upon the value of $\tilde{x}$ which can be achieved. H can be conserved as $\tilde{x}$ grows large by virtue of u^2 becoming large. On the other hand, for $\tilde{w}_z < 0$, the particle sees a potential well with respect to x, and the motion in the x-direction must remain bounded, regardless of the level of stochasticity.

A. Perturbation Treatment of Resonance Islands

We first establish the location of the resonance islands; that is to say, the values of $\tilde{H}$ and $\tilde{P}_z$ for which the perturbing wave couples resonantly with the unperturbed orbits. For $\phi = 0$, $\tilde{P}_z$ is a constant of the motion. For small values of $\phi \neq 0$, we attempt to construct a new constant of the motion, p, "close" to $\tilde{P}_z$, as an assymptotic series in ϕ. We define $p \equiv \tilde{P}_z + \phi p_1 + \phi^2 p_2 + \ldots$, and assume that $\dot{p}$ is identically 0. The first order correction p_1, the only term we shall consider, then obeys the equaton

$$0 = \dot{\tilde{P}}_z(\psi_2) + \phi\left[\frac{\partial p_1}{\partial\psi_1}\dot{\psi}_1(H_0, \tilde{P}_z, \psi_1) + \frac{\partial p_1}{\partial\psi_2}\dot{\psi}_2(H_0, \tilde{P}_z, \psi_1)\right].$$

The terms $\dot{\psi}_i$, given by Eqs. (26) and (27), are to be expressed as functions of ψ_1, $\tilde{P}_z$ and the unperturbed energy $H_0 \equiv u^2/2 + \tilde{x}[\tilde{w}_y/\epsilon - \tilde{w}_z\tilde{x}/2] - \cos\psi_1$. This is accomplished by inverting the expressions for $\tilde{P}_z$ and H_0 to express $\tilde{x}$ and u as functions of $\tilde{P}_z$ and H_0. To simplify the discussion, we consider the case $\tilde{\mathbf{w}} = 0$. Adopting the notation $\Omega_i \equiv \dot{\psi}_i(H_0, \tilde{P}_z, \psi_1)$, we have $\omega_1 = u\tilde{x}$ and $\omega_2 = ku(\tilde{x}+\theta/\epsilon)$, where $u = \sigma_1\sqrt{2(H_0 + \cos\psi_1)}$ and $\tilde{x} = \sigma_2\sqrt{2(\tilde{P}_z - u)}$, $\sigma_i = \pm 1$. We replace the coordinates ψ_1 and ψ_2 with the new

coordinates $\zeta_1 \equiv \frac{1}{q(H_0,\tilde{P}_z)} \int^{\psi_1} d\psi_1 \Omega_2/\Omega_1$ and $\zeta_2 \equiv \psi_2$, where the winding number q is given by $q(H_0,\tilde{P}_z) \equiv \frac{1}{2\pi} \oint d\psi_1 \omega_2/\omega_1$. The integrals are taken along the unperturbed orbits, and $\oint$ denotes the integral over a complete period of the unperturbed motion. Eq. (45) then becomes

$$\frac{1}{q(H_0,\tilde{P}_z)} \frac{\partial p_1}{\partial \zeta_1} + \frac{\partial p_1}{\partial \zeta_2} = Q(H_0,\tilde{P}_z,\zeta_1,\zeta_2),$$

where $Q \equiv -\dot{\tilde{P}}_z/(\phi\omega_2) = k\theta\epsilon^{-1}\omega_2^{-1} \sin\zeta_2$. Defining ζ_1 to be 0 when $\psi_1 = 0$, Q may be written as the Fourier series $Q = \sum_{m=0}^{\infty} Q_m(H_0,\tilde{P}_z)[\sin(m\zeta_1+\zeta_2) - \sin(m\zeta_1-\zeta_2)]$, whence the solution for p_1 may be written

$$p_1 = -\sum_{m=0}^{\infty} Q_m(H_0,\tilde{P}_z) \left[\frac{\cos(m\zeta_1+\zeta_2)}{1+m/q} + \frac{\cos(m\zeta_1-\zeta_2)}{1-m/q}\right].$$

For $m \geq 1$, $Q_m(H_0,\tilde{P}_z) = \frac{1}{2\pi}\frac{k\theta}{\epsilon}\int_0^{2\pi} d\zeta_1 \cos(m\zeta_1)/\Omega_2(H_0,\tilde{P}_z,\zeta_1)$. The perturbation treatment breaks down in the vicinity of the resonances, where $m + qn = 0$, $n = \pm 1$.

To approximate the island widths, we make the usual assumption that each island is well isolated from all other islands and, in the vicinity of a particular (m,n) resonance, we can replace the expression $\dot{\tilde{P}}_z = -\phi\Omega_2 Q$ with the single-harmonic approximation $\Delta\dot{\tilde{P}}_z = -\phi n \Omega_2 Q_m|_R \sin(m\zeta_1 + n\zeta_2)$, where $m = 0,1,2,\ldots$ and $n = \pm 1$. $Q_m|_R$ denotes the value of $Q_m(H_0,\tilde{P}_z)$ at the resonant values of $\tilde{P}_z$ and H_0, and $\Delta\tilde{P}_z$ is the deviation of $\tilde{P}_z$ away from resonance. Terms which can be demonstrated to be of order $\phi^{3/2}$ have been dropped. Defining $\xi \equiv m\zeta_1 + n\zeta_2$, the time-derivative of ξ is given, to lowest order in ϕ, by $\dot{\xi} = -\Delta\tilde{P}_z[\partial q/\partial\tilde{P}_z]_R\Omega_2/m$. Combining this with the expression for $\Delta\dot{\tilde{P}}_z$, one obtains $(d\Delta\tilde{P}_z)n\delta\tilde{P}_z = d\xi\phi m \sin\xi[Q_m/(\partial q/\partial\tilde{P}_z)]_R$, which may be integrated to give the familiar pendulum description of the islands:

$$\frac{\Delta\tilde{P}_z^2}{2} + A_{m.n}\cos\xi = \text{const.},$$

where

$$A_{m,n} \equiv \frac{\phi m}{n} \left[\frac{Q_m}{\frac{\partial q}{\partial \tilde{P}_z}} \right]_R .$$

Taking the separatrix, whose half-width is given by $\Delta\tilde{P}_z = 2\sqrt{|A_{m,n}|}$, as an indication of the extent of an island, we define the overlap criterion for a pair of resonances (m,n) and (m',n') as

$$S \equiv \frac{2\left[\sqrt{|A_{m,n}|} + \sqrt{|A_{m',n'}|}\right]}{\left|\tilde{P}_{z_{m,n}} - \tilde{P}_{z_{m',n'}}\right|}.$$

Here, $\tilde{P}_{z_{m,n}}$ is the value of $\tilde{P}_z$ at the (m,n) resonance.

We have worked out a numerical example of the S parameter for comparison with the numerical integration of the equations of motion. We consider the case where $\theta = .1$, $\epsilon = .03$, $k = 1$, and $\tilde{\mathbf{w}} = 0$. The Poincaré surfaces of section of Figs. 3a and 3b were calculated with these parameters and show points in the $(\psi_1, \tilde{x})$-plane as the orbits cross the surface $\psi_2 = 0 \bmod 2\pi$, with positive value of u. The energy is fixed at $\tilde{H} = 2$. With this choice of parameters, the separatrix of the corresponding unperturbed problem belongs to the class of separatrices labeled ϵ in Figs. 1k and 8. The total energy is small enough in comparison with the wave potential that the constant $v_\parallel$ approximation of Sec. IIc. fails quantitatively, despite the qualitative similarity in the appearence of the orbits to those of the pendulum. We examine an $(m,n) = (1,1)$ island and an $(m,n) = (2,1)$ island which can be seen in the lower portion of the figures, among the passing orbits. From the definition of q, we calculate that the $m = 1$ resonance occurs at $\tilde{P}_z = 3.4$, and the $m = 2$ resonance at $\tilde{P}_z = 2.7$. The "potential well" strengths A for these two islands are calculated from the above formulae to be $A_{1,1} = -.30\phi$ and $A_{2,1} = .035\phi$, from which one obtains an overlap criterion $S = 2.1\sqrt{\phi}$. Figs. 3a and 3b have values of ϕ equal to .1 and .16, respectively, yielding overlap parameters of roughly $S = .6$ and $S = .8$. For the case of $\phi = .1$, some stochasticity appears between the $m = 1$ and $m = 2$ islands, but

there appear to remain preserved K.A.M. tori separating these two resonance regions. For $\phi = .16$, the $m = 2$ island has been all but lost in the stochastic sea, and no preserved tori remain separating the two regions.

B. Global Stochasticity Estimates

The above calculation of the overlap parameter S provides reasonably detailed information concerning the transition to stochasticity. However, the calculation is unwieldy, especially since the unperturbed orbits apparently can not be described by known analytic functions. We would like to have at our disposal a simpler means of predicting the appearence of global stochasticity. In this section, we provide a more rough-and-ready estimate of the conditions under which global stochasticity can be expected to occur. We adopt the view that strong stochasticity can be expected when the primary separatrices associated with each of the two waves begin to touch. We expect that if the separatrices due to the first wave considered in isolation are well removed from the separatrices of the second wave considered in isolation, then minimal stochasticity will be present. We wish to find an overlap criterion which is defined to be equal to 1 when two separatrices are just touching (or rather would be just touching if each separatrix were constructed ignoring the effect of the other wave). Since there is a whole host of separatrices (a continuous one-parameter family corresponding to the curve of Fig. 8), we must make the notion of overlap more precise. Consider a particle which has initial conditions such that if ϕ_2 were set equal to 0, it would be at the maximal x-value of a separatrix due to the first wave. We consider this separatrix to "just touch" a separatrix of the second wave if a particle started with identical initial phase space coordinates would fall on the minimal x-value of a separatrix of the second wave, if only that wave were present. Under such conditions, we anticipate strong interaction between the resonances of the two waves and the presence of

a significant degree of global stochasticity.

To simplify the problem, we again restrict our attention to the case $\mathbf{w} = 0$. As shown in Sec. IIb., the full width of the separatrix κ of Fig. 1a is given by $\sqrt{32L_s v_0/\omega_{ce}}$. This width, which, except for a factor of $\sqrt{32}$, equals ϵL_s, is the characteristic distance used in defining our dimensionless coordinates and scales as $\phi^{1/4}$. This fourth-root scaling suggests that for small wave potential, the resonance overlap criteria should display stronger ϕ-dependence in the low kinetic energy regime than one would glean from the standard pendulum approximation. This transition from $\phi^{1/2}$ scaling to $\phi^{1/4}$ scaling is illustrated well by the separatrix of type α in Fig. 1b. One easily calculates the full width of the separatrix to be

$$\Delta x = \left[8L_s\omega_{ce}^{-1}\sqrt{2/m_e}\left(\sqrt{H+e\phi}-\sqrt{H-e\phi}\right)\right]^{1/2}.$$

For $H \gg e\phi$, the assymptotic behavior of the width is given by

$$\Delta x = 4\left[-L_s e\phi/(\omega_{ce}m_e v_\parallel)\right]^{1/2}.$$

At the minimum value of H for which this type of separatrix occurs, namely $H = e\phi$, the full width is given by

$$\Delta x = 4\left[\frac{L_s}{\omega_{ce}}\sqrt{e\phi/m_e}\right]^{1/2}.$$

In Table II we have compiled the values of the x-extrema for the various separatrices of the $\lambda = 0$ problem, along with the values of $v_\parallel$ attained at the x-extrema.

Let us first consider the conditions under which two separatrices of type κ are just touching, in the sense discussed above. The parallel velocity at the x-extremum of the separatrix associated with the i^{th} wave is given by $-2\sqrt{e\phi_i/m_e}$. Matching these velocities for both waves requires that $\phi_1 = \phi_2 \equiv \Phi$. The distance between the rational surfaces

associated with the two waves is given by θL_s, where θ is the angle between the k-vectors. Therefore, if the quantity

$$S_{\kappa\kappa} \equiv \frac{1}{\theta}\sqrt{\frac{32}{\omega_{ce}L_s}\sqrt{\frac{e\Phi}{m_e}}}$$

is equal to 1, then a particle with initial conditions $\psi_1 = \psi_2 = 0$, $v_{\|} = -2\sqrt{e\Phi/m_e}$, $x = \sqrt{8L_s/\omega_{ce}\sqrt{e\Phi/m_e}}$ would be on one separatrix if $\phi_1 = \Phi$, $\phi_2 = 0$, and would be on the other separatrix if $\phi_2 = \Phi$, $\phi_1 = 0$. We take $S_{\kappa\kappa}$ to be an overlap criterion for the restricted case of this type of separatrix. For $S_{\kappa\kappa} \ll 1$, these two web-like separatrices are well-removed from one another. We emphasize that this overlap criterion makes sense only for the case $\phi_1 = \phi_2$. Since the orbits of type κ, β, and δ all have extremal velocities of $-2\sqrt{e\phi/m_e}$, a similar constraint applies if we seek overlap criteria among pairs of these orbit types.

From Table II, one sees that for the α type separatrices $v_{\|\max} < -2\sqrt{e\phi/m_e}$. For the **g** class, $v_{\|\max} > -2\sqrt{e\phi/m_e}$. Therefore, if $\phi_2 < \phi_1$, we can find conditions for a type α separatrix associated with the second wave to touch a type γ separatrix associated with the first wave. Let p_1 and p_2 be the particle's value of $\tilde{P}_z$ with respect to the two waves. Matching the value of $v_{\|\max}$ one obtains the relation $2\sqrt{\phi_2}\sqrt{1+p_2^2/4} = \sqrt{\phi_1}p_1$, or $p_1 = \sqrt{(4+p_2^2)\phi_2/\phi_1}$. From the allowed ranges of p_1 and p_2, one obtains the condition upon ϕ_2/ϕ_1:

$$0 < \frac{\phi_2}{\phi_1} < \frac{1}{1+p_2^2/4}.$$

From Table II and the above relation between p_1 and p_2, we find that the α and γ separatrices just touch if

$$S_{\alpha\gamma} \equiv \frac{1}{\theta}\sqrt{\frac{2}{\omega_{ce}L_s}\sqrt{\frac{e\phi_2}{m_e}}}\left\{\sqrt{p_2 + 2(1+p_2^2/4)^{1/2}} + 2(1+p_2^2/4)^{1/4}\right\}$$

equals 1. Here, p_2 is permitted to be in the range $-2\sqrt{\phi_1/\phi_2 - 1} < p_2 < 0$.

Replacing the parameter p_2 by the parameter

$$A \equiv -\frac{p_2}{2\sqrt{\frac{\phi_1}{\phi_2} - 1}},$$

where the allowed range for A is $0 < A < 1$, $S_{\alpha\gamma}$ may be written

$$S_{\alpha\gamma} = \frac{\phi_1^{1/4}}{\theta}\sqrt{\frac{2}{\omega_{ce}L_s}\sqrt{\frac{e}{m_e}}}\quad G\left(\frac{\phi_2}{\phi_1}, A\right),$$

where

$$G(\phi, A) \equiv \sqrt{2\sqrt{\phi(1-A^2)+A^2} - 2A\sqrt{1-\phi}} + 2\left[\phi(1-A^2)+A^2\right]^{1/4}.$$

For a given value of ϕ_2/ϕ_1, one obtains a continuous set of overlap parameters corresponding to the value of A. This reflects the fact that many orbits are of the same class. For each value of ϕ_2/ϕ_1, one may find the maximum value of G with respect to A. Denoting this maximal function by $\bar{G}(\phi_2/\phi_1)$, one finds that $\bar{G}$ varies only between 2 and 3.4 over the domain $0 < \phi_2/\phi_1 < 1$.

Performing a similar calculation, we find that a type δ separatrix associated with wave 1 just touches a type α separatrix associated with wave 2 if

$$S_{\delta\alpha} \equiv \frac{\phi_1^{1/4}}{\theta} v\sqrt{\frac{2}{\omega_{ce}L_s}\sqrt{\frac{e}{m_e}}}\left\{\sqrt{2+p_1} + \sqrt{2-2\sqrt{1-\frac{\phi_2}{\phi_1}}}\right\}$$

equals 1, where $\phi_2 < \phi_1$. Even for large values of θ, one can make $S_{\delta\alpha} = 1$ by selecting an appropriate value of p_1. This is a reflection of the fact that the δ class of islands are centered about values of x ranging from $\pm\sqrt{L_s v_0/\omega_{ce}}$ to $\pm\infty$. This suggests that for the $\tilde{H} = 1$ torus (on which the δ type orbits occur), the overlap parameter may not be a meaningful quantity. For the $\lambda = 0$ problem, the $\tilde{H} = 1$ torus appears to be a pathological case which is particularly susceptible to the stochastic instability. This issue is discussed further in the next section.

The overlap criteria discussed in this section are somewhat problematic. The expressions diverge as θ approaches 0, which would suggest a large amount of stochasticity for small θ. This is a spurious result, since the equations of motion become integrable as θ vanishes and the waves coalesce. However, from the numerical experiments we have performed, a value of S equal to 1 appears to be a sufficient condition for the appearence of global stochasticity.

Figs. 4a and 5a show Poincaré surfaces of section for cases in which the parameters were chosen in order to yield a value of $S_{\alpha\gamma} = 1$. In both cases, the plots show the branch $u > 0$. For Fig. 4a we chose $\theta/\epsilon = 4.06$, $k = 1$, $\tilde{H} = 0$, $\tilde{\mathbf{w}} = 0$, and $\phi = .5$. For these parameters, the separatrix of the corresponding unperturbed problem belongs to the class γ, the figure-eight separatrix of Fig. 1l. The unperturbed problem thus contains orbits which are qualitatively distinct in character from those occuring in the large $v_{\|}$, pendulum approximation. For Fig. 5a the parameter values were $\theta/\epsilon = 4.828$, $k = 1$, $\tilde{H} = 1$, $\tilde{\mathbf{w}} = 0$, and $\phi = 1$. As Fig. 8 indicates, the unperturbed version of this case ($\tilde{H} = 1$ torus) has not one, but a continuous set of infinite-period orbits of types β and δ. This example thus contains a non-universal feature which is typically absent from similar two degree-of-freedom systems investigated in previous works.

Figs. 4a and 5a both point to the complete destruction of a second isolating integral of the motion, when $S = 1$. In Figs. 4b and 5b, the same cases were run as in Figs. 4a and 5a, respectively; except that the perturbation parameter ϕ was reduced to .01. One sees that a high level of stochasticity remains. The persistence of such a large degree of stochasticity at even a one percent perturbation level is quite remarkable. Again, the $\tilde{H} = 1$ torus appears to be highly vulnerable to the stochastic instability.

C. The Special Role of the H=1 Torus

Refering again to Fig. 8, consider a particle with initial conditions such that it initially falls on the curve γ in the $(\tilde{P}_z, \tilde{H})$-plane. As mentioned previously, in the absence of the perturbation ($\phi \equiv \phi_2/\phi_1 = 0$), the orbit is represented by a stationary point in this projection. For $\phi \neq 0$, the point is free to move horizontally in the $(\tilde{P}_z, \tilde{H})$-plane, but not vertically. We expect an orbit lying near the locus of separatrices of the unperturbed problem to be subject to the stochastic instability. But in light of the K.A.M. theorem, one expects that, for small enough perturbations, the orbit will remain bounded by nested preserved K.A.M. tori. The horizontal motion in the $(\tilde{P}_z, \tilde{H})$-plane is thus restricted for small perturbations.

If one were to add a third wave (or toroidal geometry) to the problem, the added time dependence, not removable through coordinate transformation, would destroy the invariance of the Hamiltonian. The added mobility of the particle in the vertical direction in the $(\tilde{P}_z, \tilde{H})$-plane would enable a particle starting on the γ curve to move along a "corridor" in the vicinity of the locus of separatrices. This is the Arnold diffusion. Even for small perturbations, very large excursions can take place in action space, under these circumstances.

Now consider an orbit starting on one of the curves β or δ. These are exceptional cases, since these curves lie parallel to the $\tilde{P}_z$ axis. Even with only two waves present, the particle apparently has the oportunity to travel along this "corridor" of separatrices, while still strictly conserving the value of $\tilde{H}$. For the $H = 1$ torus, every orbit with a value of $\tilde{P}_z$ between 0 and ∞ is a homoclinic orbit, and is, hence, susceptible to the stochastic instability. We conjecture that, for this special region of phase space, something akin to Arnold diffusion occurs for the two-wave problem, and that even for small perturbations,

a particle could eventually diffuse to large values of $\tilde{P}_z$. We have no *a priori* reason to believe there is anything preventing it from doing so. The growth of $\tilde{P}_z$ to large values does not, however, imply that $v_{||}$ becomes large. The parallel velocity for the $\mathbf{w} = 0$ problem is restricted by the conservation of the Hamiltonian. The canonical momentum $\tilde{P}_z$ is permitted to attain a large value by virtue of the coordinate $\tilde{x}$ becoming large.

In numerical experiments, we have attempted to confirm the above observations regarding the peculiar nature of the $\tilde{H} = 1$ torus by integrating the orbits for an ensemble of 640 particles. All particles were started with identical initial values of $\tilde{H}$ and $\tilde{P}_z$, but distributed randomly in ψ_1 and ψ_2. In Figs. 9a and 9b, we have plotted, as a function of time, the root-mean-square deviation in the value of $\tilde{P}_z$, i.e. $\left[\left\langle \tilde{P}_z^2 \right\rangle - \left\langle \tilde{P}_z \right\rangle^2\right]^{1/2}$, where the angle brackets denote the ensemble average. For both of the illustrated examples, Eqs. (24)–(27) were integrated with $\tilde{\mathbf{w}} = 0$, $\phi = .2$, $\theta/\epsilon = .1$, and $k = 1$. For Fig. 9a, the initial conditions were $\tilde{H} = 0$, $\tilde{P}_z = \sqrt{2}$. These orbits would, in the absence of the perturbation, thus fall on the curve γ of Fig. 8. As time increases, the packet of particles spreads with respect to the value of $\tilde{P}_z$. But, as one would expect, the standard deviation of $\tilde{P}_z$ eventually saturates as the ensemble fills up the stochastic layer in the neighborhood of the unperturbed problem's separatrix. Fig. 9b illustrates the case $\tilde{H} = 1$, $\tilde{P}_z = 2$. These initial conditions correspond to to the point κ of Fig. 8. The qualitative behavior of the ensemble is qualitatively different from that of the former example. We detect no evidence of saturation and the behavior is consistent with our conjecture that a kind of diffusion in $\tilde{P}_z$ takes place.

V. Conclusions

This work examines the motion of electrons in two electrostatic plane waves in a slab magnetic field geometry with shear. We show that the drift orbits are described by a

two degree-of-freedom, autonomous Hamiltonian system. A conserved energy confines each orbit to a three-dimensional manifold in phase space. Each energy surface is topologically equivalent to a toroidal volume. Our dynamical system is thus quite similar to the field-line problem in toroidal confinement devices, except that here we have one complete toroidal system for each value of the conserved energy.

With only one wave present, the existence of a symmetry direction leads to a conserved canonical momentum P_z, and the motion can be reduced to quadrature. The motion on homoclinic trajectories may be expressed in terms of elliptic integrals, but the general one-wave orbits do not appear to admit analytic solutions in terms of well-known functions.

In the limit of large parallel kinetic energy, we show that the two-wave system becomes equivalent to the pendulum subjected to a time-dependent perturbation, a system which has been exhaustively studied by others. In this work, we have focused our attention upon the regime in which the electron's parallel kinetic energy and potential energy are comparable and the pendulum approximation ceases to be valid.

In this low parallel velocity regime, the separatrices have characteristic widths which are on the order of $\sqrt{L_s v_0/\omega_{ce}}$, where v_0 is the trapping velocity. This width scales as the fourth root of the wave potential as contrasted with the pendulum separatrix widths which scale as the square root of the potential. This difference in scaling suggests that for small wave amplitude, the low energy electrons, when subjected to the second perturbing wave, may display an early onset of stochasticity in comparison with those electrons in the pendulum regime.

In addition to this quantitative difference in scaling, the low kinetic energy regime displays qualitatively different behavior. A much richer variety of unperturbed orbit classes

occur in the small energy regime. We have provided a comprehensive catalogue of all possible orbit classes, for any combination of parameter values. In our analysis of the unperturbed motion, we have found that for a given value of the conserved canonical momentum, chains of elliptic and hyperbolic fixed points are located at values of the radial coordinate satisfying a cubic equation. For canonical momenta less than $3/2m_e(\omega/k_y)^{2/3}v_0^{1/3}$, one chain of X and O points exists. For P_z greater than this value, the chain bifurcates into three chains of fixed points. Depending upon the parameter ranges and value of P_z, these fixed points may be tied together in a variety of topologically distinct ways, including a web-like homoclinic trajectory connecting all three chains.

For values of canonical momentum exceeding a certain positive value, which depends upon the wave's phase velocity, three disjoint chains of pendulum-like islands occur. (Here, the direction of positive P_z is the direction of the current j_z.) The central chain is located close to the rational surface and for large P_z, may be identified with the positive $v_\parallel$ pendulum separatrix occuring in the ususal constant $v_\parallel$ approximation. The other two island chains, located on either side of the rational surface, are a new feature of the low energy regime, being entirely absent in the constant $v_\parallel$ approximation. As P_z is made large, the distance of these two island chains from the rational surface increases without bound. In the opposite limit of large negative canonical momentum (P_z antiparallel to j_z), there appears only the usual single chain of islands near the rational surface.

In light of these features of the low energy regime, one expects far greater resonant interaction of the two waves than the usual constant $v_\parallel$ approximation would permit. In the constant $v_\parallel$ approximation, all regions of resonant trapping are spatially localized near the rational surface. If the rational surfaces of the two waves are well-separated, resonant interaction simply doesn't take place. In contrast, for the low energy regime, resonance

trapping occurs at arbitrary radial distance from the rational surface (insofar as we have ignored the radial structure of the modes) and spatial coincidence of trapping regions associated with the two waves takes place regardless of the separation of the rational surfaces. Again, this leads to an enhanced level of stochasticity for low energy electrons. Numerical integration of the equations of motion and examination of Poincaré surfaces of section has confirmed our expectations that the low parallel velocity regime is especially fragile to the onset of chaos.

We have undertaken an examination of diffusion rates by numerically integrating the evolution of an ensemble of several hundred particles. In Sec. IVc., we compared the temporal behavior of the spread in the canonical momentum for two different values of energy. Our investigations of radial diffusion rates are too preliminary to be included here. We can, however, make some statements concerning the scaling of the diffusion rates. Assuming that under conditions of global stochasticity the radial motion can be characterized as a diffusive process, one can calculate a dimensionless radial diffusion coefficient $\tilde{D}_x$ as a function of the ensemble distribution and the dimensionless parameters $\{\tilde{w}_y/\epsilon, \phi, k, \theta/\epsilon, \tilde{w}_z\}$. From the definitions of the dimensionless quantities $\tilde{x}$ and $\tilde{t}$, we then know that the diffusion coefficient D_x in real units must scale as $\left[\left(L_s^2 k_{1y}^4 c^6 \phi_1^5 m_e\right)/(eB_0^6)\right]^{1/4}$ or $\left(\frac{m_e}{m_i}\right)^{1/4} \frac{cT_e}{eB_0} k_{1y}\rho_s \left(\frac{L_s}{\rho_s}\right)^{1/2} \left(\frac{e\phi_1}{T_e}\right)^{5/4}$ times the dimensionless number $\tilde{D}_x$. In future work we will investigate the validity of the diffusion approximation and the parametric dependence of $\tilde{D}_x$ on the dimensionless parameters of the two-wave Hamiltonian system.

Acknowledgments

The authors gratefully acknowledge the interest and suggestions of Dr. F.L. Hinton during the course of this work. The research was supported in part by the U.S. Department of Energy under contract DE-FG05-53088.

References

1. W. Horton, *Handbook of Plasma Physics, vol. II*, ed. A.A. Galeev and R.N. Sudan, (North-Holland, Amsterdam, 1984), pp. 383–449.
2. T.M. O'Neil, Phys. Fluids **8**, 2255 (1965).
3. T.H. Dupree, Phys. Fluids **10**, 1049 (1967).
4. S.P. Hirshman and K. Molvig, Phys. Rev. Lett. **42**, 648 (1979).
5. R.G. Kleva and J.F. Drake, Phys. Fluids **27**, 1686 (1984).
6. W. Horton, Plasma Physics **27**, 937 (1985).
7. B.V. Chirikov, Phys. Reports **52**, 263 (1979).
8. D.F. Escande, Phys. Reports **121**, 165 (1985).
9. J.M. Greene, J. Math. Phys. **20**, 1183 (1979).
10. P. Terry and W. Horton, Phys. Fluids **26**, 106 (1983).
11. S.P. Hirshman **23**, 562 (1980).
12. B.V. Chirikov, Phys. Reports **52**, 347 (1979).
13. V.I. Arnold, *Mathemetical Methods of Classical Mechanics*, (Springer-Verlag, New York, 1978), p. 407.
14. W.M. Nevins, J. Harte, and Y. Gell, Phys. Fluids **22**, 2108 (1979).
15. R.G. Littlejohn, J. Plasma Phys. **29**, 111 (1983).
16. V.I. Arnold, *Mathemetical Methods of Classical Mechanics*, (Springer-Verlag, New York, 1978), pp. 243–244.
17 A.B. Rechester and T.H. Stix, Phys. Rev A **19**, 1656 (1979).
18. D.I. Choi and W. Horton, Phys. Fluids **20**, 628 (1977).

Table 1

	n Even	n Odd
$\zeta_1 > 1$	Stable	Unstable
$0 < \zeta_2 < 1$	Unstable	Stable
$\zeta_3 < 0$	Stable	Unstable

Table 2

Orbit Type	Parameter Range	$x_{\max}$	$v_{\parallel_{\max}}$
α	$\tilde{P}_z < 0$	$\pm\sqrt{2}\epsilon L_s\sqrt{\tilde{P}_z + 2(1+\tilde{P}_z^2/4)^{1/2}}$	$-2v_0\sqrt{1+\tilde{P}_z^2/4}$
β	$0 < \tilde{P}_z < 2$	$\pm\sqrt{2}\epsilon L_s\sqrt{2+\tilde{P}_z}$	$-2v_0$
γ	$0 < \tilde{P}_z < 2$	$\pm 2\epsilon L_s\sqrt{\tilde{P}_z}$	$-v_0\tilde{P}_z$
δ	$\tilde{P}_z > 2$	$\pm\sqrt{2}\epsilon L_s\sqrt{2+\tilde{P}_z}$	$-2v_0$
ϵ	$\tilde{P}_z > 2$	$\pm\sqrt{2}\epsilon L_s\sqrt{\tilde{P}_z - 2(\tilde{P}_z^2/4-1)^{1/2}}$	$2v_0\sqrt{\tilde{P}_z^2/4-1}$
κ	$\tilde{P}_z = 2$	$\pm\sqrt{8}\epsilon L_s$	$-2v_0$

Figure Captions

Fig. 1 Orbit classes for the one-wave problem. Plots show projections of orbits upon $(\psi_1, \tilde{x})$-plane for constant value of P_z.[4pt]

Fig. 2 The toroidal structure of the constant-energy surface. The poloidal and toroidal directions corespond to $\mathbf{k}_1 \cdot \mathbf{x}$ and $\mathbf{k}_2 \cdot \mathbf{x}$, respectively. The minor radius corresponds with $\exp(u + \tilde{x}^2/2)$.

Fig. 3 Poincaré surfaces of section for $\tilde{H} = 2$, $\theta = .1$, $\epsilon = .03$, $k = 1$, and $\mathbf{w} = 0$. $\phi = .1$ in (a), and $\phi = .16$ in (b).

Fig. 4 Poincaré surfaces of section for $\tilde{H} = 0$, $\theta/\epsilon = 4.06$, $k = 1$, and $\mathbf{w} = 0$. $\phi = .5$ in (a), and $\phi = .01$ in (b).

Fig. 5 Poincaré surfaces of section for $\tilde{H} = 1.0$, $\theta/\epsilon = 4.828$, $k = 1$, and $\mathbf{w} = 0$. $\phi = 1.0$ in (a), and $\phi = .01$ in (b).

Fig. 6 Atlas of one-wave orbit classes. Letters a through l label the regions of the $(\lambda = \tilde{w}_y/\epsilon, \tilde{P}_z)$-plane which produce the corresponding orbit topologies of Figs. 1a – 1l.

Fig. 7 Plot of the curve $b = (\zeta^2 + 2\zeta^{-1})/3$, where $b \equiv 2/3\lambda^{-2/3}\tilde{P}_z$ and $\zeta \equiv \lambda^{-1/3}\tilde{x}$. This curve yields, for each given value of $\tilde{P}_z$ the radial location of the fixed points.

Fig. 8 Locus of the separatrices for the one wave system, taking $\mathbf{w} = 0$.

Fig. 9 Standard deviation in $\tilde{P}_z$ as a function of time for ensemble of 640 particles. Parameter values are $\theta/\epsilon = .1$, $\phi = .2$, $k = 1$, $\mathbf{w} = 0$. Particles initially distributed randomly in phase with $\tilde{H} = 0$, $\tilde{P}_z = \sqrt{2}$ (a), and $\tilde{H} = 1$, $\tilde{P}_z = 2$ (b).

Table Captions

Table 1 Stability of the fixed points occuring at $\psi_1 = n\pi$ and $\tilde{x} = (\tilde{w}_y/\epsilon)^{1/3}\zeta$. The ζ_i are the 3 roots to the cubic equation (37).

Table 2 Properties of separatrices for $\mathbf{w} = 0$, one-wave system. Letters $\alpha - \kappa$ correspond to curve labels of Figs. 1 and 8. Listed are allowed ranges of $\tilde{P}_z$, radial extrema, and values of parallel velocity at radial extrema for respective separatrix classes.

Fig. 1

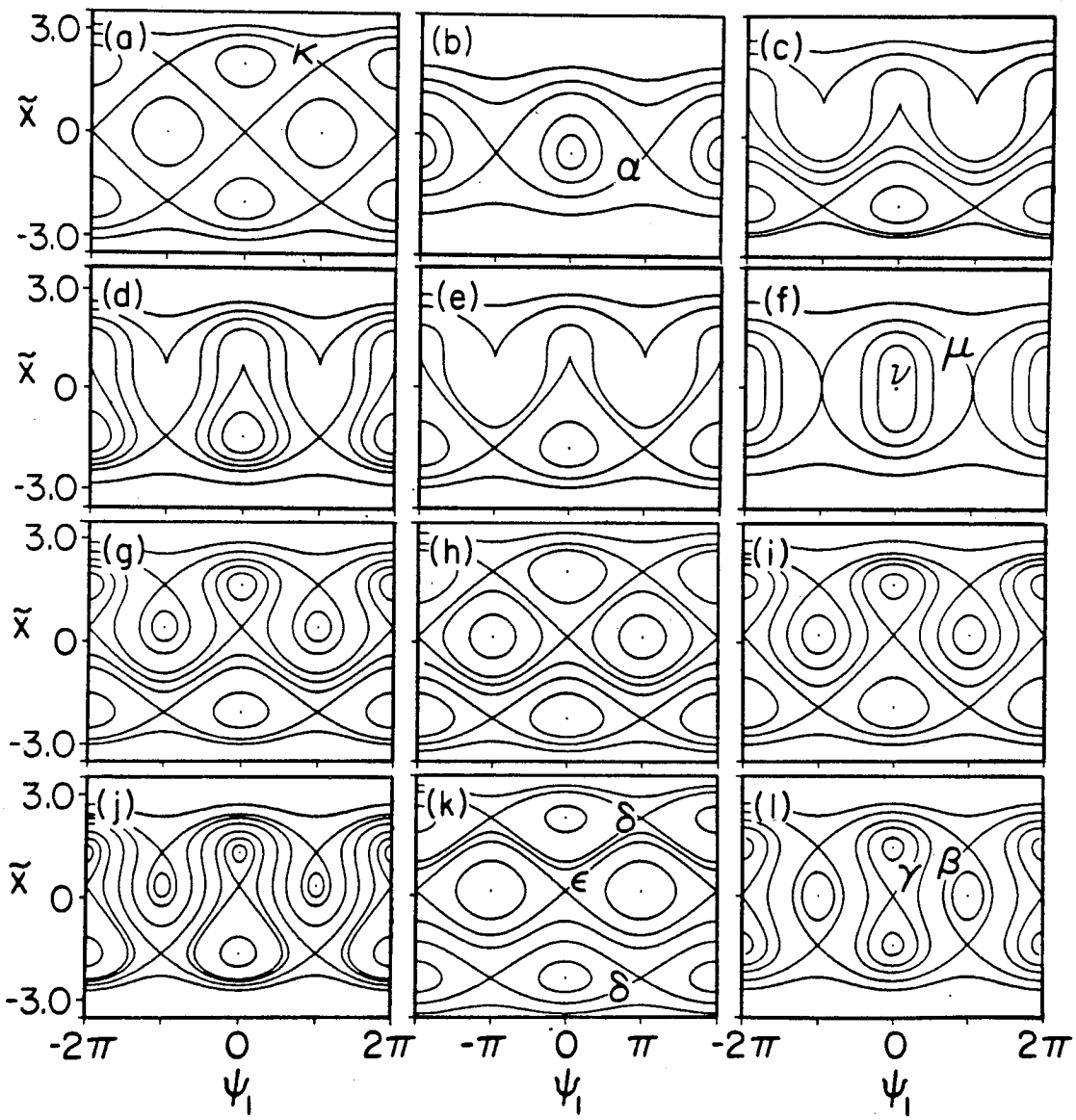

Fig. 2

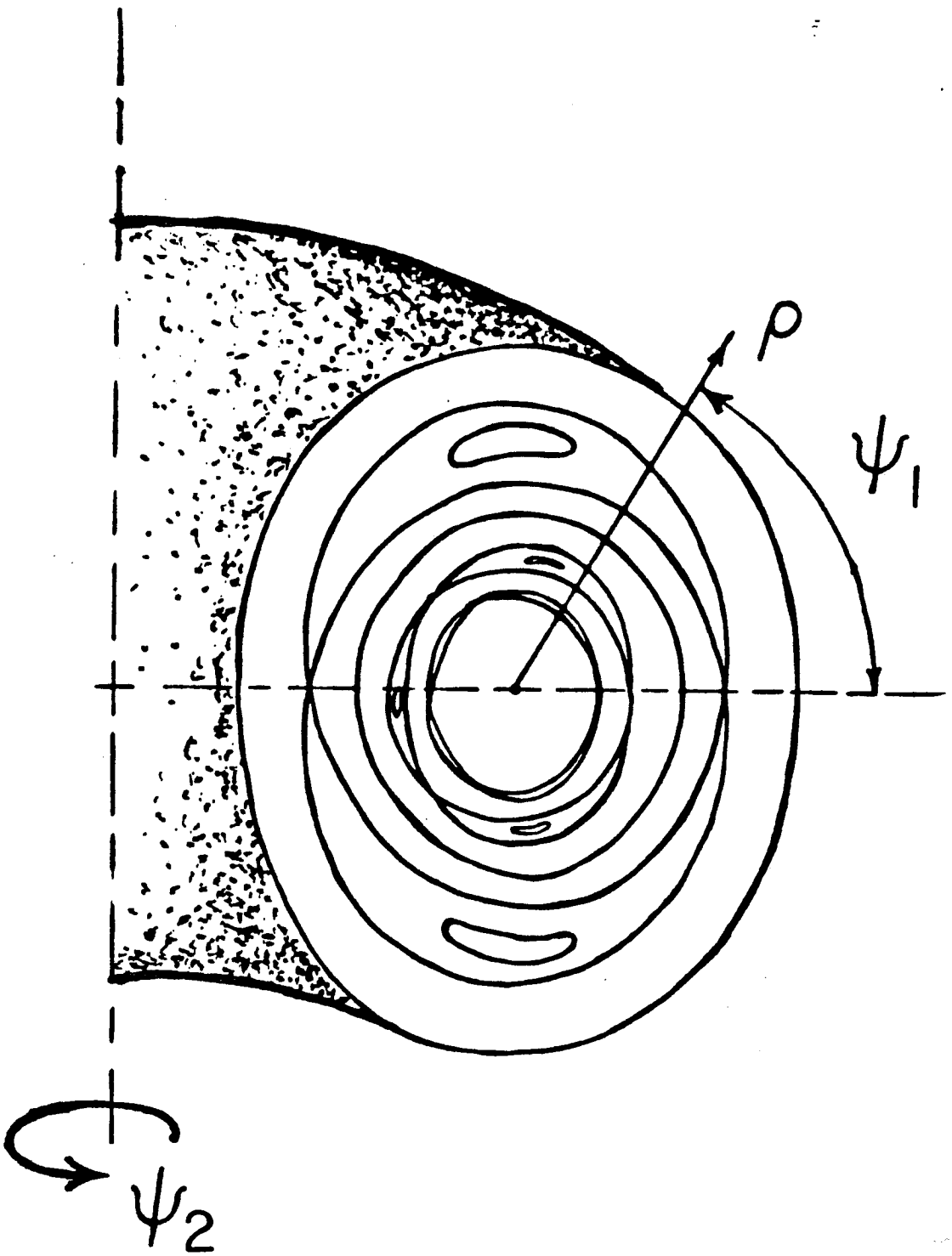

Fig. 3

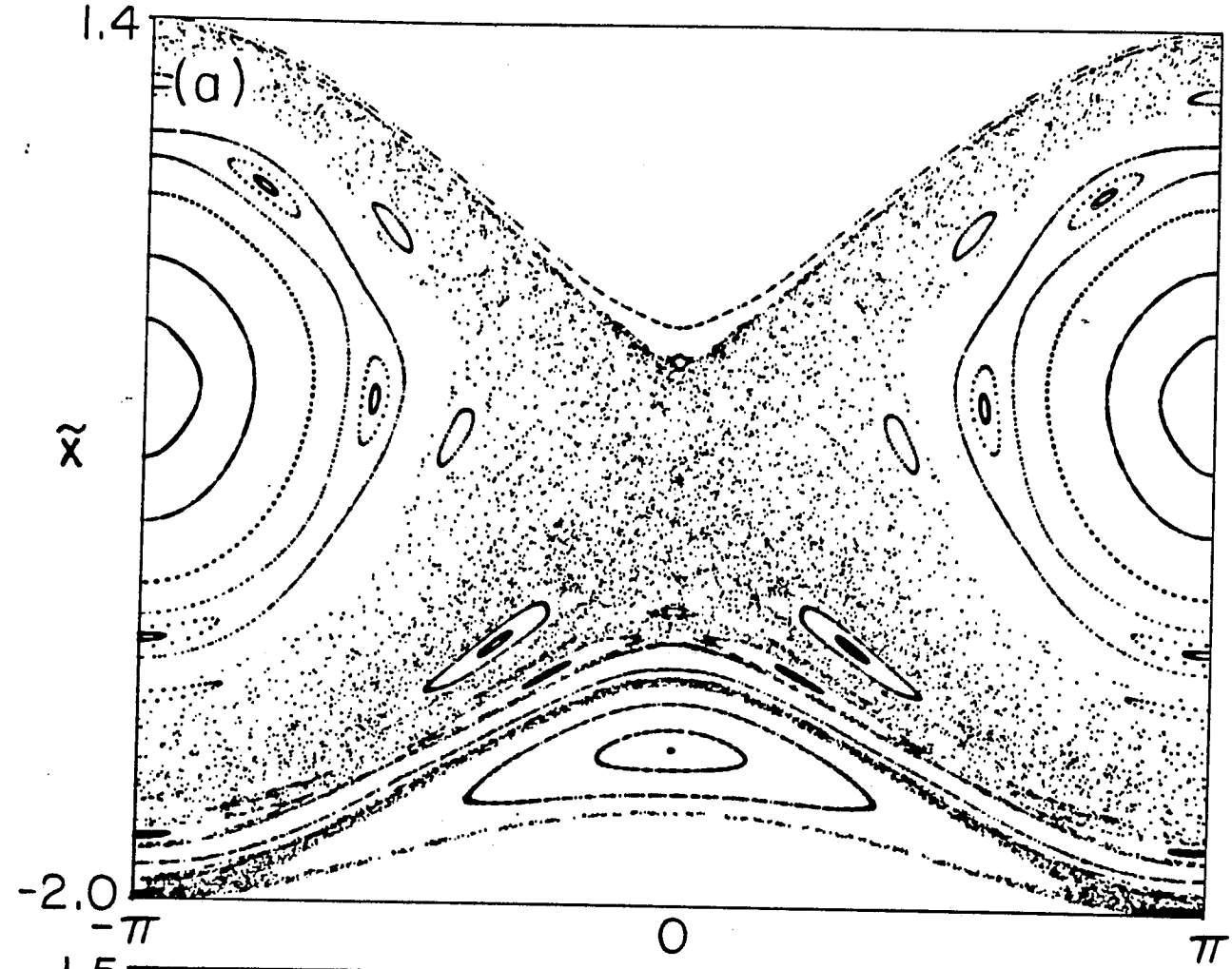

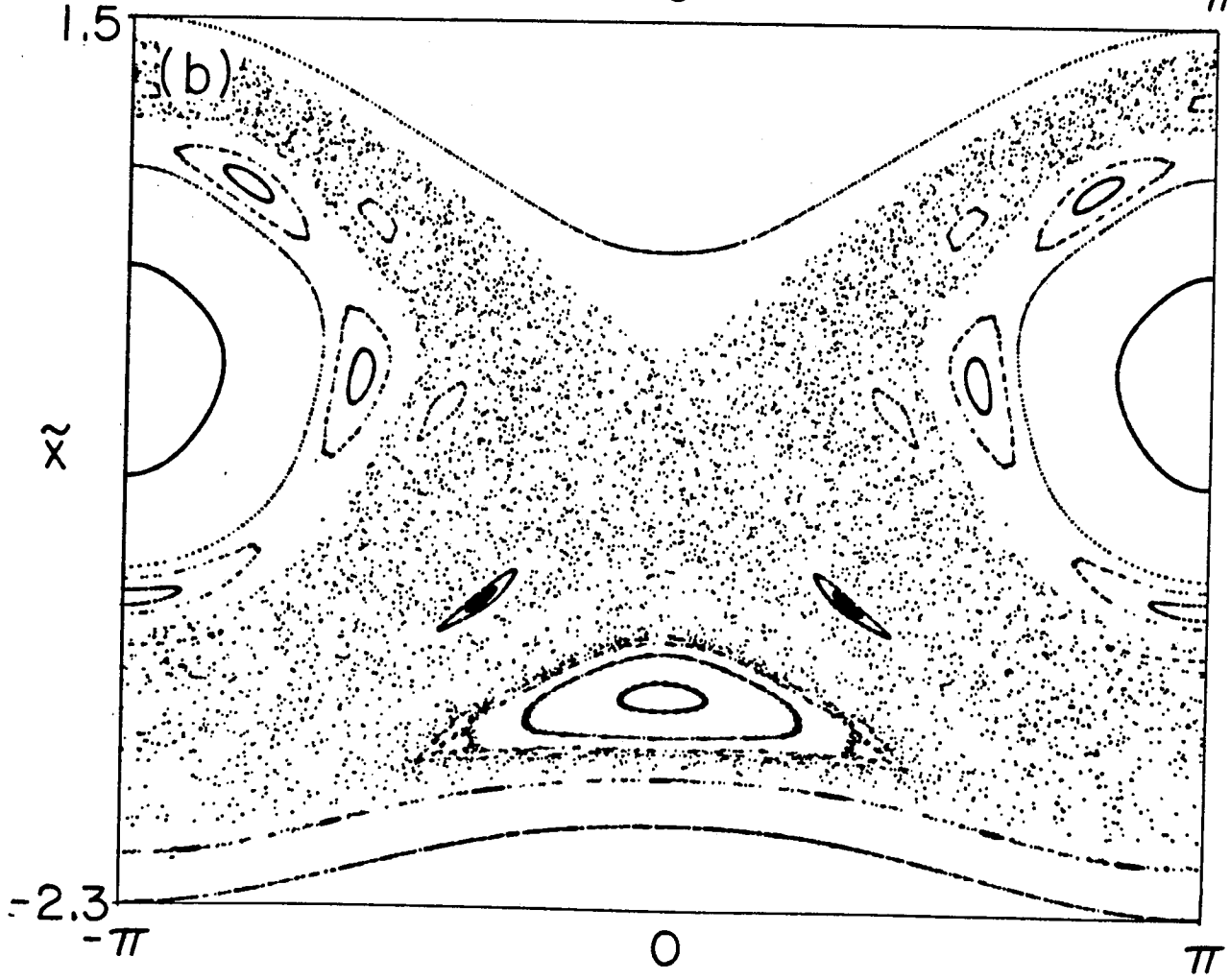

Fig. 4

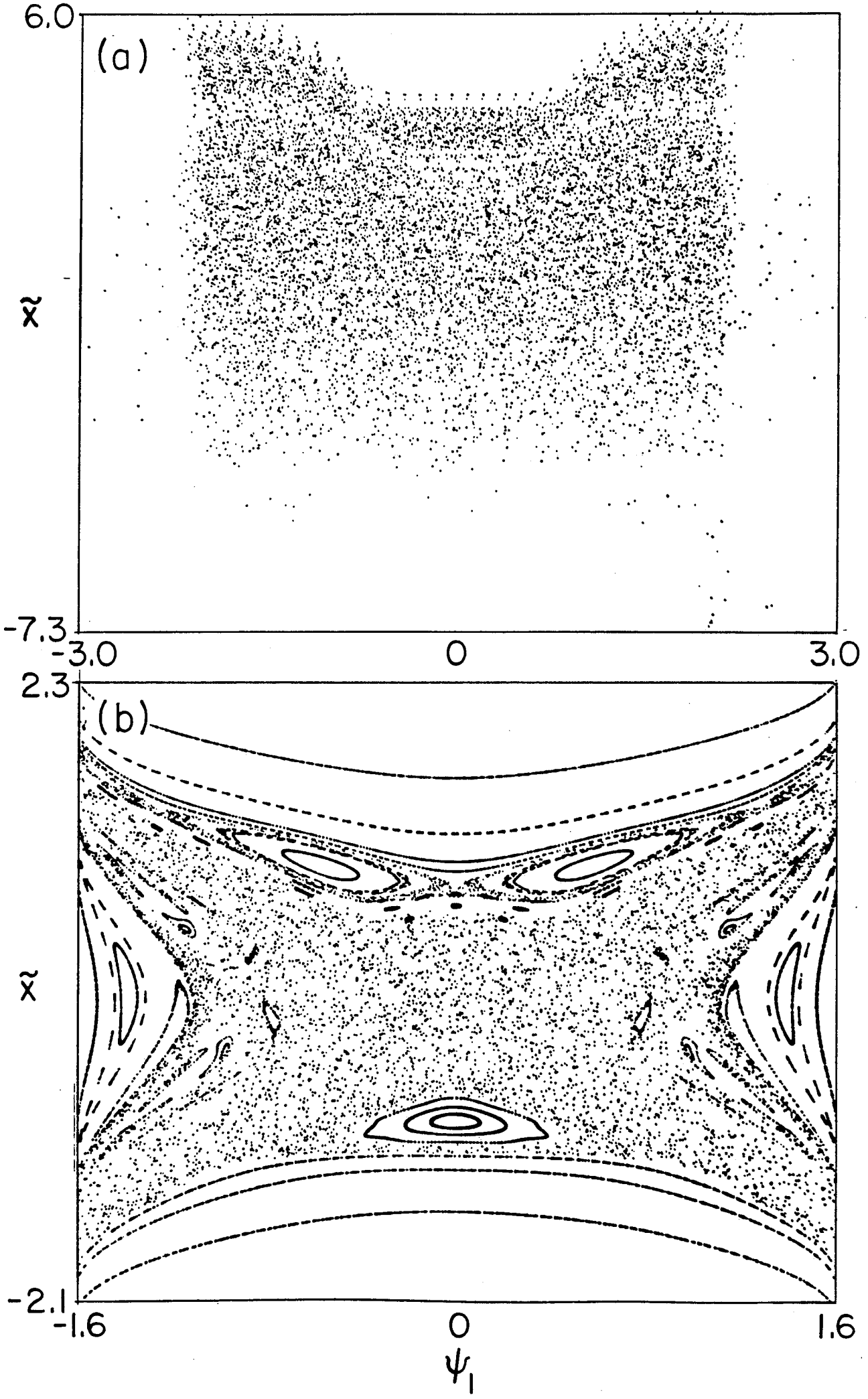

Fig. 5

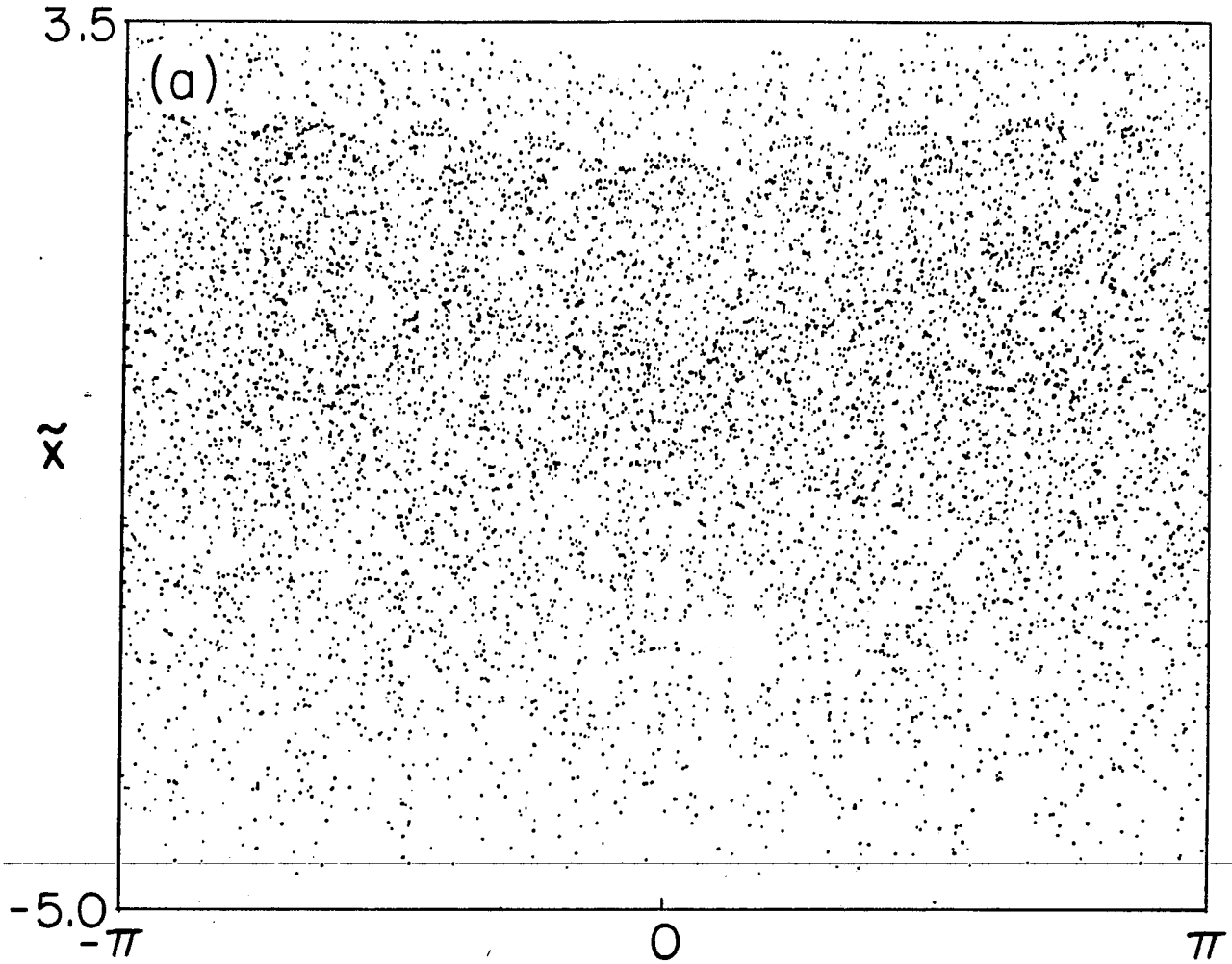

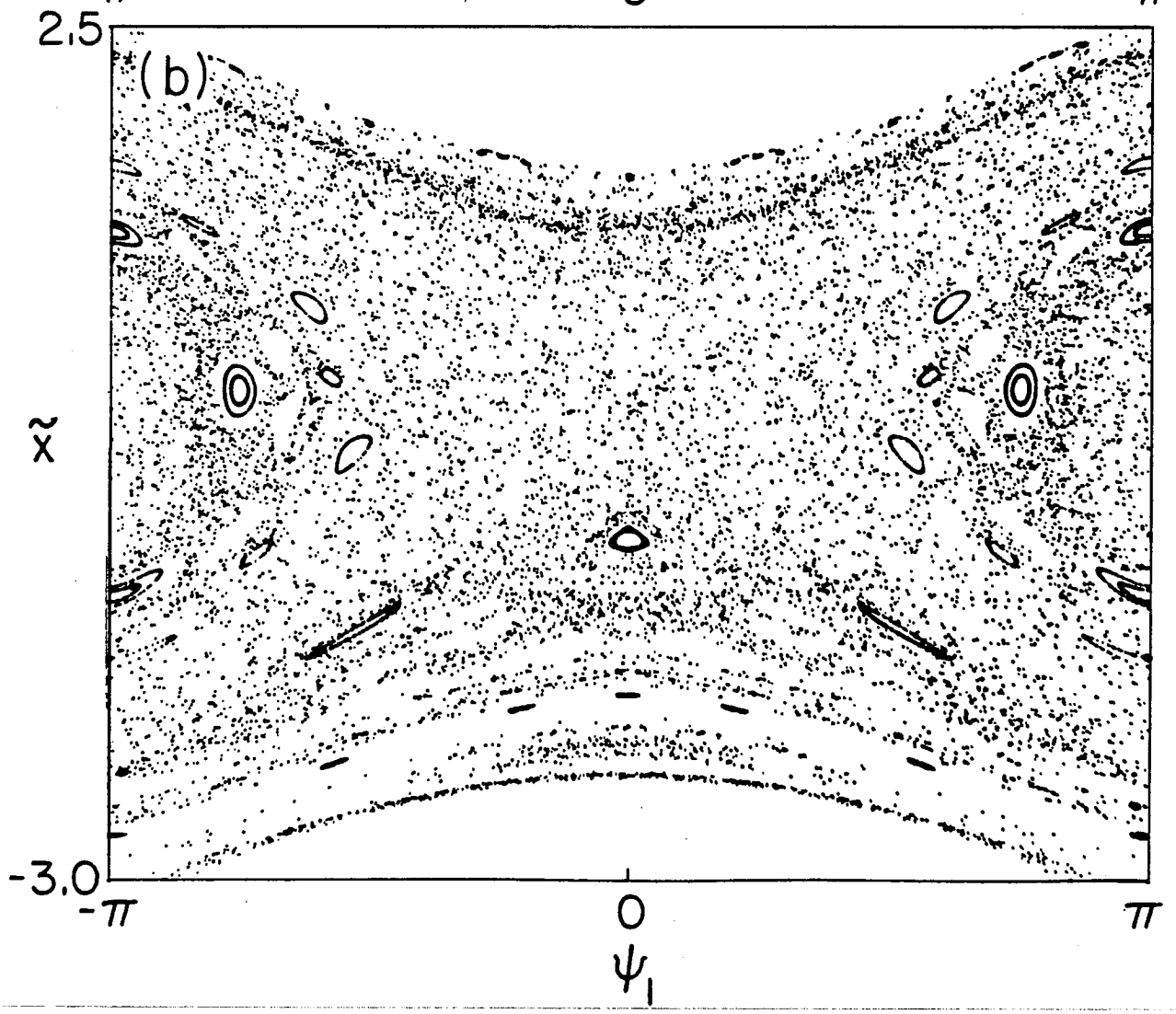

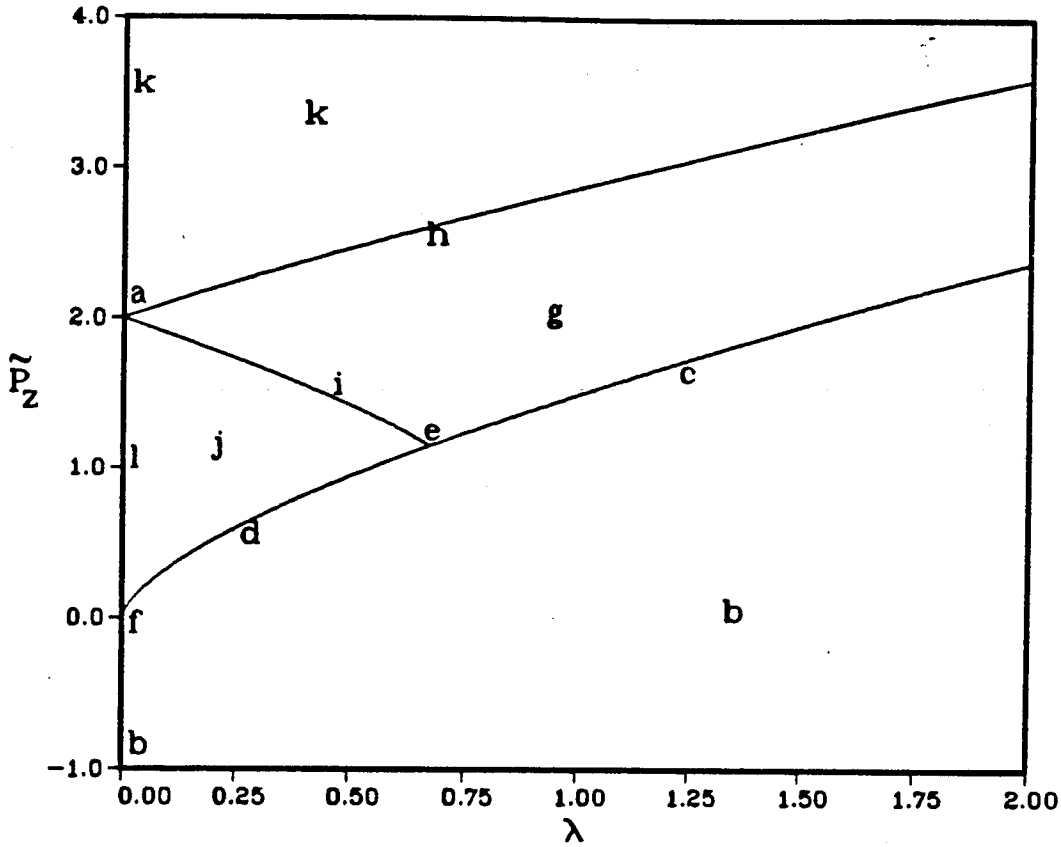
4.0
3.0
2.0
1.0
0.0
−1.0
$\tilde{P}_z$
k
k
h
a
g
j
c
e
l
j
d
f
b
b
0.00
0.25
0.50
0.75
1.00
1.25
1.50
1.75
2.00
λ

Fig. 6

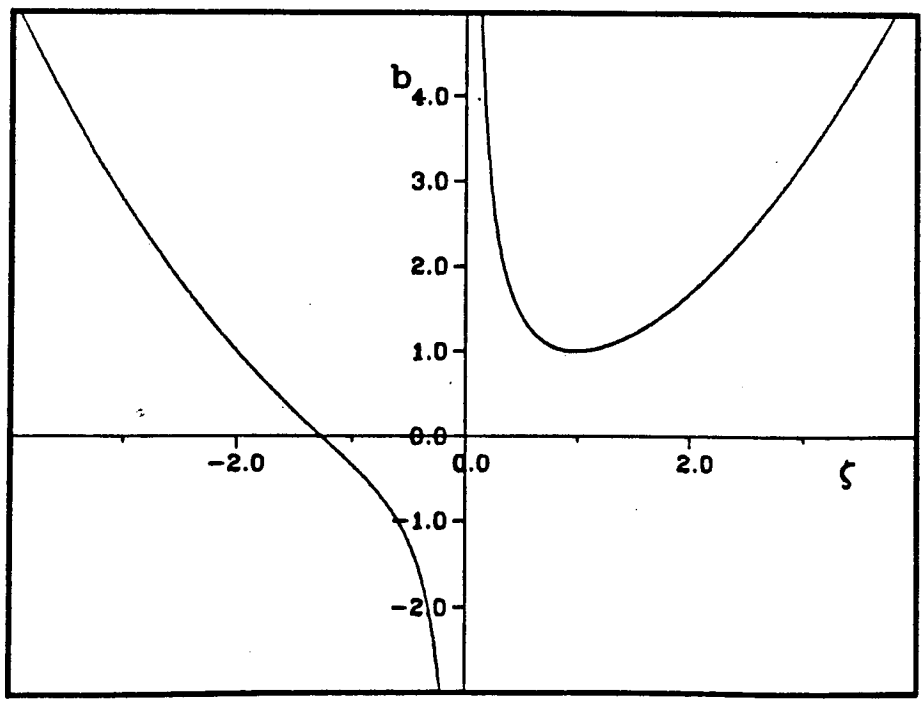
b
4.0
3.0
2.0
1.0
0.0
−1.0
−2.0
−2.0
0.0
2.0
ζ

Fig. 7

Fig. 8

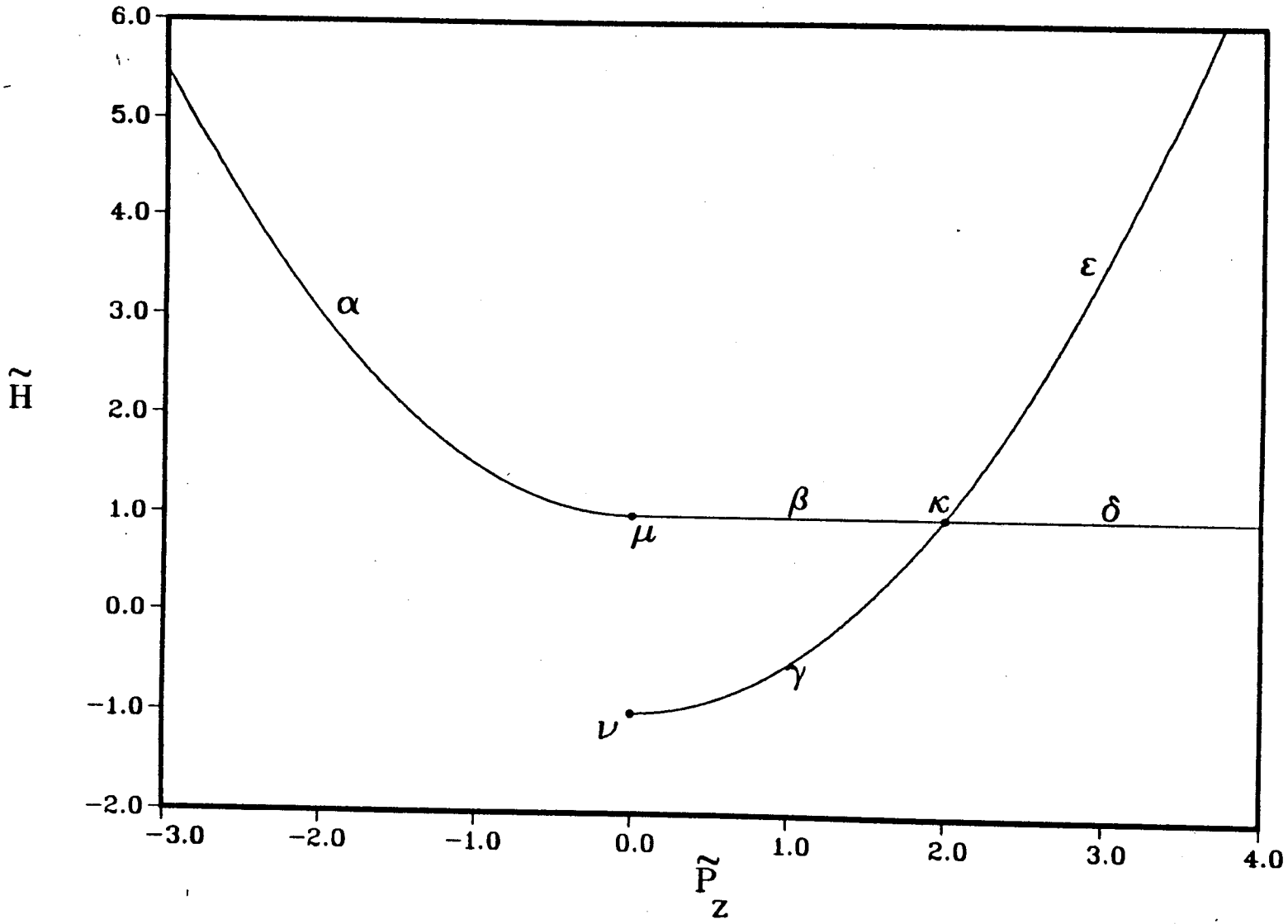
6.0
5.0
4.0
3.0
2.0
1.0
0.0
−1.0
−2.0
$\tilde{H}$
−3.0
−2.0
−1.0
0.0
1.0
2.0
3.0
4.0
$\tilde{P}_z$
α
β
γ
δ
ε
μ
ν
κ

Fig. 9

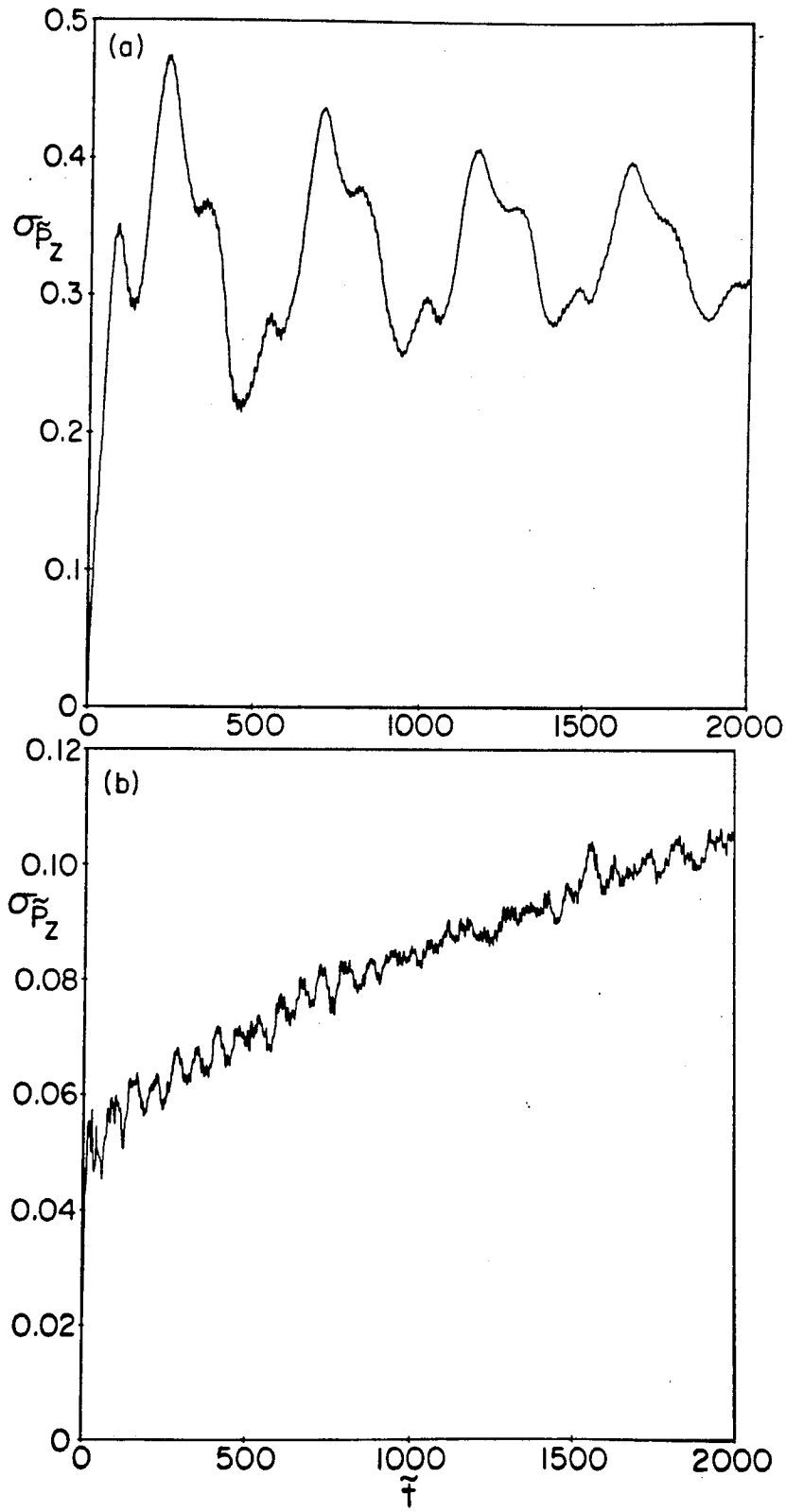
(a)
0.5
0.4
$\sigma_{\tilde{p}_z}$
0.3
0.2
0.1
0
0
500
1000
1500
2000
(b)
0.12
0.10
$\sigma_{\tilde{p}_z}$
0.08
0.06
0.04
0.02
0
0
500
1000
1500
2000
$\tilde{t}$